Journal of Alloys and Compounds 739 (2018) 1065–1079

Contents lists available at ScienceDirect

Journal of Alloys and Compounds

journal homepage: http://www.elsevier.com/locate/jalcom

Evidence of magnetoelectric coupling in $0.9BiFeO_3$-$0.1Ba[Ti_{0.95}(Yb_{0.5}Nb_{0.5})_{0.05}]O_3$ ceramic

A. Amouri [a, *], S. Aydi [a], N. Abdelmoula [a], H. Dammak [b], H. Khemakhem [a]

[a] Laboratoire des Matériaux Multifonctionnels et Applications (LaMMA), Université de Sfax, Faculté des Sciences de Sfax (FSS), Route de Soukra, km 3.5, B.P.1171, 3000, Sfax, Tunisia

[b] Ecole Centrale de Paris, Laboratoire Structures, Propriétés et Modélisation des Solides, UMR 8580 CNRS, Grande Voie des Vignes, 92295, Châtenay-Malabry, France

ARTICLE INFO

Article history:
Received 30 July 2017
Received in revised form
4 December 2017
Accepted 10 December 2017
Available online 28 December 2017

Keywords:
$BiFeO_3$
Magnetoelectric coupling
Multiferroic
Mössbauer
Raman spectroscopy

ABSTRACT

The physical properties of the Multiferroïc lead-free $0.9BiFeO_3$-$0.1Ba[Ti_{0.95}(Yb_{0.5}Nb_{0.5})_{0.05}]O_3$ ceramic were investigated by in-situ Mössbauer spectroscopy, X-ray diffraction (XRD), dielectric measurements and Raman scattering. Both $BiFeO_3$ and $0.9BiFeO_3$-$0.1Ba[Ti_{0.95}(Yb_{0.5}Nb_{0.5})_{0.05}]O_3$ ceramics underwent in-situ Mössbauer spectroscopy in the temperature range of 300 K to 653 K and the parameters of hyperfine interactions were determined. The magnetic transition temperature T_N of our doped sample was of 568 K, which was lower than that of $BiFeO_3$. This reduction of T_N originated from the presence of different exchange constants resulting from the weakening of $J_{Fe\text{-}Fe}$. The deviation of the reduced magnetic hyperfine field H(T)/H(0) as a function of the reduced temperature T/T_N from the Brillouin curve of Fe^{3+} ($S = 5/2$) for the three sextets and the determination of the critical exponent β, of 0.375 ± 0.022 in the range of $0.01 < 1\text{-}T/T_N < 0.5$ revealed a 3D magnetic long range order phase transition. The complexity of the spatial spin structure was a result of the canting of antiferromagnetically ordered spins of $BiFeO_3$. Our findings revealed the effect of the non-magnetic substituents Ba and Yb/Nb/Ti in A and B sites, respectively on the magnetic properties. Around the magnetic transition temperature, both isomer shift evolution and quadruple splitting distribution showed pronounced anomalies associated with the onset of magnetic ordering. The Debye temperature (θ_D) was deduced to be of 257 ± 21 K. These results revealed $0.9BiFeO_3$-$0.1Ba[Ti_{0.95}(Yb_{0.5}Nb_{0.5})_{0.05}]O_3$ as a promising material for piezoelectric devices. XRD analyses were performed for temperatures from 300 K up to 750 K. Gradual structural evolution, as temperature increased, exhibited an isostructural phase transition and an anomaly in the evolution of lattice parameters and the unit cell volume as well as a significant shift in the atomic positions near the magnetic transition temperature T_N. These behaviors indicate magnetoelastic coupling. The temperature dependence of the real part of dielectric permittivity and dielectric loss (tan δ) was investigated over a wide range of temperatures at 1 kHz. During its evolution, an anomaly was observed at 568 K; which corresponded to the magnetic transition temperature T_N. Raman scattering spectra were measured in the temperature range from 303 K to 728 K. Drastic changes, especially that of the three two-phonon modes centered at around 1000-1500 cm^{-1}, were the results of magnetic rearrangement and atomic displacement leading to both modulating magnetic exchange interaction and polarization state. All these results prove the magnetoelectric coupling of $0.9BiFeO_3$-$0.1Ba[Ti_{0.95}(Yb_{0.5}Nb_{0.5})_{0.05}]O_3$ ceramic.

1. Introduction

Recently, a growing attention has been oriented to multiferroïc materials that showed magnetoelectric coupling due to the presence of both magnetic and ferroelectric orders at the same temperature. The magnetoelectric coupling between electric dipoles and magnetic ones translating the effect of electric poling on magnetic hysteresis loop and the change in dielectric constant with an external magnetic field [1,2,18] is useful to numerous innovative technological applications [3–5] and underling novel physical phenomena [5–8]. Unfortunately, ferroelectricity and magnetism tend to be mutually exclusive; and even in instances of coexistence,

* Corresponding author.
E-mail address: amouri.amira00@gmail.com (A. Amouri).

https://doi.org/10.1016/j.jallcom.2017.12.101
0925-8388/

the interaction between the order parameters are usually indirect and the microscopic origin of both phenomena are weakly interfering [7]. Nevertheless, the sensitivity of the dielectric properties at the magnetic transition temperature is an evidence of magnetoelectric coupling [17,18]. Such an observation is strongly related to structural phase diagrams. In this context, a goal of this work was to deeper understand structural evolution which seems challenging because of the vast space structures of artificially synthesized magnetoelectric materials, especially in order to have ferroelectric and ferromagnetic orders at room temperature [6]. By far, the perovskite $BiFeO_3$ (BFO) is one of the most well studied among the multiferroïc materials seen that it presents a coupling between the magnetic and electric ordering at room temperature (high ferroelectric Curie point (T_c ~ 1103 K) and G-type Antiferromagnetic Neel temperature (T_N ~ 643 K) [11,12]. At room temperature, Bulk $BiFeO_3$ crystallizes in a Rhomboedral distorted perovskite structure with an *R*3*c* space group. The Bi 6s lone pair electrons are responsible for ferroelectricity and the partially filed d orbitals of Fe lead to a magnetic moment [12,13,18]. A growing interest [9,10] has been made to realize the magnetic structure highlighted as the canted G-type antiferromagnetic order of Fe^{3+} ions with a spatially-modulated spin with a large period of $\lambda = 620$ Å [10]. In fact, Each Fe^{3+} ion is surrounded by six Fe^{3+} nearest neighbors with antiparallel moments leading to this spiral magnetic moments arrangement in this $BiFeO_3$ structure as a result of Dzyloshinsii–Moriya (DM) interaction. This interaction causes a slight deviation from ideal antiferromagnetic behavior giving rise to weak ferromagnetism in $BiFeO_3$ [11,12]. This inhomogeneous spin structure leads to the cancelation of macroscopic magnetization which prohibits the observation of a linear magnetoelectric effect [13]. This incommensurate space spin structure has been reported to be modulated by many factors [14–21]: application of strong magnetic field [19], substitution of Bismuth and/or iron by other element in A and B sites, respectively [14–21], leading to the increase of the resistivity resulting in the improvement of electric and magnetic properties [14–16]. The effect of this factors has widely been investigated in order to better understand the link between the modification of the structures and each electric and magnetic properties change and to achieve pronounced ferroelectric, piezoelectric and magnetic properties [17–21].

In this context, in our previous studies [25], we have proved the amelioration of both electrical and magnetic properties of $BiFeO_3$, for the system $(1\text{-}x)BiFeO_3\text{-}xBaTi_{0.95}(Yb_{0.5}Nb_{0.5})_{0.05}O_3$ with compositions $0 \leq x \leq 0.3$ [25]. The choice of this material system was based on research results done by Abdelkafi et al. [60] on $BaTi_{1-x}(Nb_{0.5}Yb_{0.5})_xO_3$ ceramics that showed that $BaTi_{0.95}(Yb_{0.5}Nb_{0.5})_{0.05}O_3$ is a classical ferroelectric material exhibiting excellent electrical properties: a high dielectric permittivity of about 11420 at 1 kHz at $T_c = 358$ K [60] better than $BaTiO_3$ (ε'_r around 9000 and $T_c = 457$ K) [26]. The magnetic order was further investigated by discussing the factors contributing to the amelioration of magnetization, as the rate of substitution increased, at room temperature [25]. These factors are the canting angles proved by XRD Riveted refinement data, the modulation of cycloid spin structure confirmed by ^{57}Fe Mössbauer spectroscopy, the presence of Fe^{2+} detected by X-ray photoelectron (XPS) and also the effect of grain size observed by scanning electron microscope (SEM) [25]. All these results prove the importance of the study of temperature dependence on $0.9BiFeO_3\text{-}0.1Ba[Ti_{0.95}(Yb_{0.5}Nb_{0.5})_{0.05}]O_3$ ceramic of electric and especially magnetic properties, seen that its spatially spin cycloid is just modulated: not completely suppressed [25].

In this article, we focus on the temperature dependence of the structural, dielectric and magnetic properties of a $0.9BiFeO_3\text{-}0.1Ba[Ti_{0.95}(Yb_{0.5}Nb_{0.5})_{0.05}]O_3$ sample, as a synthesized ceramic, by the analysis and interpretation of data obtained from XRD, in-situ Mössbauer spectroscopy, dielectric measurements and Raman scattering characterizations showing magnetoelectric coupling.

2. Experimental techniques

The preparation of polycrystalline undoped $BifeO_3$ and doped $0.9BiFeO_3\text{-}0.1BaTi_{0.95}(Yb_{0.5}Nb_{0.5})_{0.05}O_3$ ceramic samples was carried out using the solid state reaction method. Stoichiometric amounts of (Bi_2O_3 - 99.9% purity, Aldrich), Barium carbonate ($BaCO_3$ - 99.9% purity, Aldrich), Titanium oxide (TiO_2 - 99.9% purity, anatase phase, Aldrich), Ytterbuim oxide (Yb_2O_3 - 99.9% purity, Aldrich), Niobium oxide (Nb_2O_5 - 99.9% purity, Aldrich), and Iron oxide (Fe_2O_3 - 99.9% purity, Aldrich) powders were thoroughly mixed with alcohol in agate mortar for 12 h, then dried, and calcined at 873 K for 12 h. A little excess amount of Bi_2O_3 was added to compensate the volatile part of Bi_2O_3 during high-temperature sintering. The ground powders were pressed into disks of 8 mm in diameter and 1 mm in thickness. The pellets were sintered at 1103 K and 1253 K, respectively, for 1 h in air. Before any characterization, the purity phases of our ceramics were checked by rapid XRD measurement.

XRD analyses were performed by using a Bruker PANalytical Empyrean diffractometer using monochromated $CuK_{\alpha 1}$ radiation ($\lambda = 1.5405$ Å) in transmission geometry. The angle range $18^\circ \leq 2\theta \leq 80^\circ$ was scanned with a step of 0.02° using an integration time of 10 s counting time for each step. At the Anton-Paar HTK-16 Room, XRD measurements were made at room temperature and after annealing in up to 750 K in order to follow the structural evolution depending on temperature for our prepared ceramic $0.9BiFeO_3\text{-}0.1BaTi_{0.95}(Yb_{0.5}Nb_{0.5})_{0.05}O_3$ ($x = 0.1$). The values of the lattice and profile parameters were determined by using a global profile-matching method with the "Fullprof" software [22]. Rietveld refinement was done for long X-ray measurements for temperatures around T_N: for T = 300 K; 550 K; 560K; 570 K and 580 K allowing the determination of the ions shift from their ideal positions.

Transmission Mössbauer measurements were performed using a conventional constant acceleration spectrometer with a ^{57}Co-in-Rh source. Mössbauer measurements were conducted on our synthesized samples in standard transmission geometry at room temperature and in-situ measurements after annealing the samples from 300 K up to 1073 K in Argon atmosphere. Both $x = 0$ and 0.1 compositions of $Bi_{(1-x)}Ba_xFe_{(1-x)}[Ti_{0.95}(Yb_{0.5}Nb_{0.5})_{0.05}]_xO_3$ powder were mixed with bore nitride, an appropriate compound of inert filler free of Mössbauer elements, in order to overcome the sample powder scarcity. The pellet of 32 mm of diameter and 1.5 mm of thickness was prepared under a pressure of 1961.33×10^5 Pa with a concentration of 10–15 mg/cm^2. Both sides of each sample were covered with aluminum to guarantee uniform temperature in all samples. A measurement time of approximately 3 days was necessary to obtain a spectrum with acceptable statistics seen that Bismuth ^{83}Bi, Barium ^{56}Ba, titane ^{81}Ti, Ytterbium ^{70}Yb and Niobium ^{41}Nb have an important electronic density compared to that of ^{26}Fe. Spectra were fitted using «Winiso 1.0» and « fulham » programs.

The dielectric measurement was performed on a ceramic disk after deposition of golden electrodes on both sides of the sample by cathodic sputtering. The area of the Au electrode and distance between electrodes were 23.23 mm^2 and 0.89 mm, respectively. At a frequency of 10 kHz, the real part of dielectric permittivity and dielectric loss ($\tan\delta$) were determined in vacuum as a function of temperature using an impedance bridge type Agilent 4284A. The temperatures were in the 303–620 K range (temperature measurement limit). All the dielectric data were collected with heating at a rate of 2 Kmin^{-1}. The room temperature P–E hysteresis loops was measured in a silicone oil bath equipped with a Sawyer–Tower

circuit and a linear variable differential transformer. The measurements were performed at a frequency of 10 Hz.

Raman spectroscopy measurements were recorded in backscattering configuration from 50 to 1500 cm^{-1} using a micro-Horiba HR 800 monochromator. The spectrometer had a wave number resolution better than 3 cm^{-1} and was equipped with a microscope (Olympus BX41), with the Helium ion laser 532 nm emission lines at a power of 15 mW and with a CDD detector. Temperature-dependent Raman spectra of sintered samples were recorded from 303 to 728 K since the spectrometer was equipped with a LinkamTHMS 600 heating/cooling stage. The experiments were repeated several times to confirm results.

3. Results and discussion

3.1. Mössbauer spectroscopy

In order to study the local atomic environment around the Mössbauer probe nuclei, Mössbauer measurements at room temperature and versus temperatures were conducted in transmission geometry for both $BiFeO_3$ (x = 0) and $Bi_{0.9}Ba_{0.1}Fe_{0.9}[Ti_{0.95}(Yb_{0.5}Nb_{0.5})_{0.05}]_{0.1}O_3$ (x = 0.1) ceramics.

At room temperature, Mössbauer spectra suggested magnetic ordering of both $BiFeO_3$ (x = 0) and $Bi_{0.9}Ba_{0.1}Fe_{0.9}[Ti_{0.95}(Yb_{0.5}Nb_{0.5})_{0.05}]_{0.1}O_3$ (x = 0.1) ceramics, as shown in Figs. 2 and 3. The spectra of doped BFO x = 0.1 composition exhibited broadened features due to the hyperfine distributions related to the local variations of the neighborhood of iron. Furthermore, the six absorption line patterns confirmed that $BiFeO_3$ is antiferromagnetic above T_N modulated with a period of 620 Å. This result is consistent with previous publications [10,11]. $BaTi_{0.95}(Yb_{0.5}Nb_{0.5})_{0.05}O_3$ substituted $BiFeO_3$ samples exhibited magnetic ordering with probably screwed or slightly antiferromagnetic ordering [25]. In fact, the spectrum that became more symmetric for $Bi_{0.9}Ba_{0.1}Fe_{0.9}[Ti_{0.95}(Yb_{0.5}Nb_{0.5})_{0.05}]_{0.1}O_3$ is an evidence of more isotropic rearrangement of different non-equivalent Fe sites in the crystal structure.

Figs. 2 and 3 show two series of in-situ Mössbauer spectra of $BiFeO_3$ (x = 0) and $Bi_{0.9}Ba_{0.1}Fe_{0.9}[Ti0_{.95}(Yb_{0.5}Nb_{0.5})_{0.05}]_{0.1}O_3$ (x = 0.1) ceramics, respectively, as a function of temperature. The evolution of Mössbauer spectra according to temperatures in the range 300–650 K allows the determination of the magnetic transition temperature. In fact, below the magnetic transition temperature, spectra showed six line patterns corresponding to the six magnetic splitting levels of the iron nuclear energy. These are characteristic of magnetically ordered Fe^{3+} moments due to the presence of a hyperfine magnetic field, which turns into doublet, above T_N, expressing paramagnetic order. In fact, with increasing temperature, Mössbauer spectra transform to one simple Lorentzion doublet with symmetrical lines that emphasize the uniformity of structural positions of iron atoms in the paramagnetic state [27]. This observed spectral shape is consistent with the transition from a spin spiral modulated structure to a paramagnetic symmetrical one. Thus, the magnetic transition temperature T_N for our ceramic compositions were estimated. $BiFeO_3$ showed a magnetic transition temperature of T_N of 643 K; which is fully compatible with previous reports [10]. For $Bi_{0.9}Ba_{0.1}Fe_{0.9}[Ti_{0.95}(Yb_{0.5}Nb_{0.5})_{0.05}]_{0.1}O_3$ (x = 0.1), this magnetic transition temperature became around 568 K. This remarkable decrease of T_N for x = 0.1, compared to undoped $BiFeO_3$, is to be noted. This shift of T_N temperature has been widely investigated for A and/or B site BFO substituted materials [27–33]. S. M. Selbach et al. [28] and K. Sen et al. [29] considered the correlation between decreasing crystallite size and that of the magnetic transition temperature. M. A. Ahmed et al. [30] discussed the basis of the variation of the T_N as a function

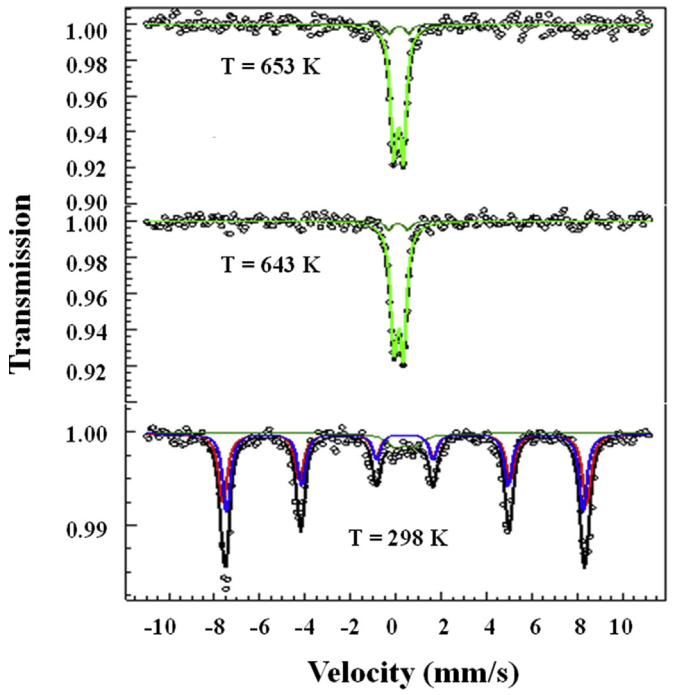

Fig. 2. In-situ Mössbauer measurements of $BiFeO_3$ (x = 0) recorded as a function of temperature.

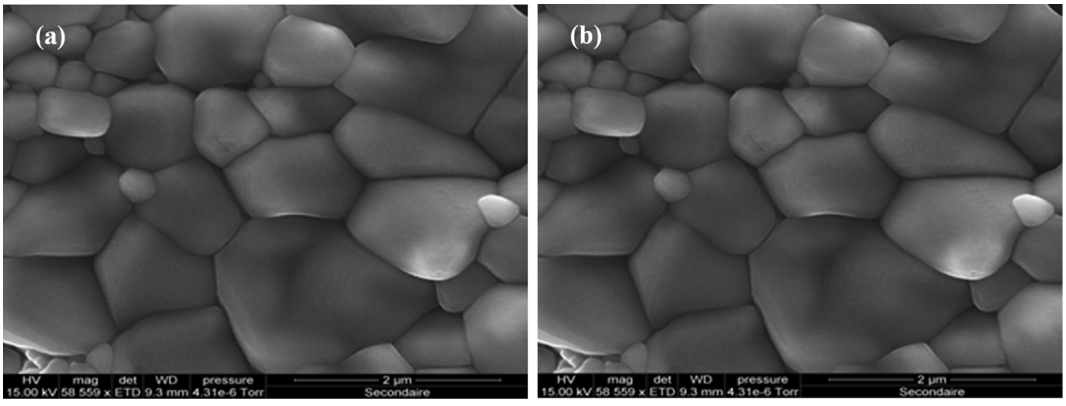

Fig. 1. SEM micrographs of (a) $BiFeO_3$ and (b) $0.9BiFeO_3$-$0.1Ba[Ti_{0.95}(Yb_{0.5}Nb_{0.5})_{0.05}]O_3$ ceramics, respectively.

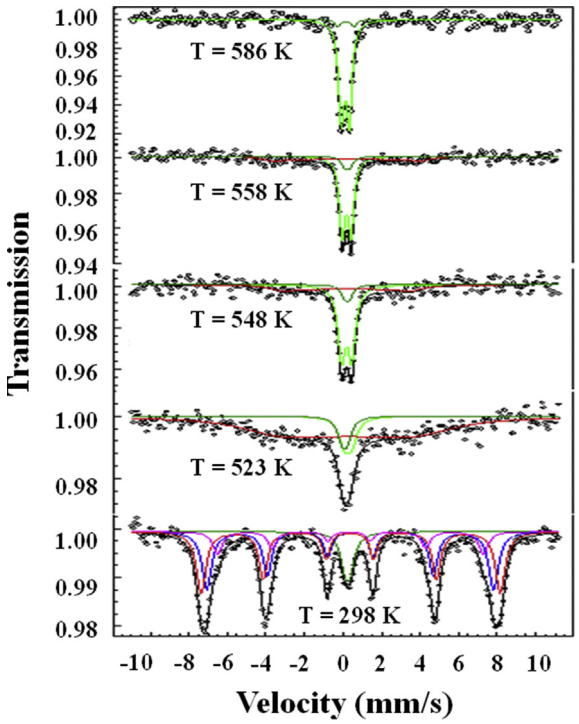

Fig. 3. In-situ Mössbauer measurements of $Bi_{0.9}Ba_{0.1}Fe_{0.9}[Ti_{0.95}(Yb_{0.5}Nb_{0.5})_{0.05}]_{0.1}O_3$ (x = 0.1) recorded as a function at selected temperatures.

of the tolerance factor. In our case, the average grain size for undoped and doped BFO is of 1.4 μm and 1.2 μm, as shown in the SEM micrographs in Fig. 1(a) and (b), of $BiFeO_3$ and $0.9BiFeO_3$-$0.1Ba[Ti_{0.95}(Yb_{0.5}Nb_{0.5})_{0.05}]O_3$ ceramics, respectively. The decrease of this crystallite size could be a factor contributing to the decrease of T_N as previously reported [29], but it is still debatable seen the μm order (not nanometric).

Yet, the increase of tolerance factor from 0.961 to 0.970 for x = 0 and 0.1 compositions, respectively, is contradictory to the correlation revealed with T_N [30]. A deeper investigation into this decrease of T_N for our doped $Bi_{0.9}Ba_{0.1}Fe_{0.9}[Ti_{0.95}(Yb_{0.5}Nb_{0.5})_{0.05}]_{0.1}O_3$ ceramic can be obtained based on the following equation [31–33]:

$$T_N = JZS(S+1)\cos\theta \quad (1)$$

where J is the magnetic exchange constant, S is the spin of Fe^{3+}, Z is the average number of linkages per Fe^{3+} ions, and θ is ⟨Fe-O-Fe⟩ band angle.

An increase in T_N is expected with the substitution of Bi and Fe by Ba and Ti/Yb/Nb in A and B sites, respectively, as a result of the increase of Fe-O-Fe band angles towards 180° as previously reported by T. Durga Rao et al. for Eu [31] and Ho [32] doped $BiFeO_3$. This phenomenon is in correlation with Rietveld refinement showing that Fe-O-Fe band angles increase from 153.3° for Rhombohedral R3C structure of our undoped BFO to Fe-O_1-Fe and Fe-O_2-Fe of 180° and 166.892° in tetragonal *P4mm* space group symmetry for the $Bi_{0.9}Ba_{0.1}Fe_{0.9}[Ti_{0.95}(Yb_{0.5}Nb_{0.5})_{0.05}]_{0.1}O_3$ sample [25]. Nevertheless, T_N decreased in our case. This unexpected result was in fact due to the weakening of the magnetic interactions rather than bond angle variation. The presence of non-magnetic $Ti^{4+}/Yb^{3+}/Nb^{5+}$ ions at Fe site weakens the magnetic interaction: B site substitution leads to the presence of different types of exchange constant J such as $J_{Fe\text{-}Ti}$, $J_{Fe\text{-}Nb}$, $J_{Fe\text{-}Yb}$, $J_{Ti\text{-}Nb}$, $J_{Ti\text{-}Yb}$, $J_{Ti\text{-}Ti}$, $J_{Nb\text{-}Yb}$, $J_{Nb\text{-}Nb}$, $J_{Yb\text{-}Yb}$ and $J_{Fe\text{-}Fe}$ between the B-sites. All these types of exchange interaction are weaker than the latter and lead to the weakening of such interactions. As a result, the weakening of J leads to a reduction in the magnetic transition temperature. Our result is similar to the study of Nd and Sc co-substituted $BiFeO_3$ reported by T. Durga Rao et al. [33].

To deeper understand the iron nucleus and surrounding interactions that lead to the evolution of modulated spin structure, investigation was based on experimental line positions and the splitting Mössbauer spectra. Each Mössbauer spectrum was fitted with adequate functions. Figs. 2 and 3 show spectrums of $BiFeO_3$ and $Bi_{0.9}Ba_{0.1}Fe_{0.9}[Ti0_{.95}(Yb_{0.5}Nb_{0.5})_{0.05}]_{0.1}O_3$ (x = 0.1), respectively. The extracted hyperfine parameters derived from the calculated spectra: isomer shift (IS), quadruple splitting (QS), and hyperfine magnetic field (Hhyp) and the average site populations are presented in Table 1. In fact, for pure $BiFeO_3$ two models are proposed for the iron ordering magnetic moments: the first considers a unique type of crystallographic position for Fe^{3+} [34,35], whereas the second assumes two nonequivalent iron positions with different magnetic moment values [36–38]. The second model was more significant, allowing an understanding of the origin of modulated spin structure indication of different trigonal distortions of the octahedral environment of both Fe-sites [36]. Above the magnetic transition temperature (T_N), $BiFeO_3$ Mössbauer spectra were fitted with two sextets (S_1; S_2) and one doublet. The sextets S_1 and S_2 are consistent with those of Rhomboedral $BiFeO_3$ and characteristic of magnetically ordered Fe^{3+} state. The quadruple splitting of doublet is attributed to the paramagnetic phase, $Bi_2Fe_4O_9$ [39] which was given a similar assignment for this component by De Sitter et al. [36]; Blaauw and Van der Woude [40] and Fischer et al. [41].

Fig. 3 shows a series of selected Mössbauer spectra obtained from in-situ measurements on $Bi_{0.9}Ba_{0.1}Fe_{0.9}[Ti0_{.95}(Yb_{0.5}Nb_{0.5})_{0.05}]_{0.1}O_3$ (x = 0.1) samples. Below the magnetic transition temperature, Mössbauer spectra were fitted with three symmetric sextets (S_1, S_2 and S_3) and one single line. At room temperature; spectra were analyzed with the three sextets and a single line. The three sextet components (S_1, S_2 and S_3) with hyperfine magnetic fields of 48 T; 47 T and 38 T are indicative of a magnetically ordered state which decreases with increasing temperature and finally collapses at a temperature above 586 K. The single line component decreased but still slightly persisted at a similar measuring temperature. The obtained spectra were then dominated by Lorentzion doublet, which highlighted the paramagnetic state. The line asymmetry of this paramagnetic doublet persisted for temperatures above T_N. This may be attributed to the distribution of quadruple splitting and/or polycrystalline anisotropy and/or a Goldanskii- Karyagin effect [42–44].

The quadruple splitting arises due to the interaction between quadruple moments of the nucleus and surrounding electric field gradients. They give relevant information about the charge symmetry around the iron nucleus. The large value of the quadruple splitting is attributed to the large distortion of Fe site [40]. Fig. 4 shows that around T_N, this hyperfine parameter shows the greatest gap value revealing the largest distortion of Fe site. The difference in the quadruple splitting values and signs is characteristic of the variation in the angles between the principal axis of the electric field and the spin direction [31]. The evolution of such an angle seems difficult to discuss pointing in the complexity of the system.

From the ^{57}Fe Mössbauer transmission spectra, the magnetic splitting resulting from the interaction between the nucleus and any surrounding magnetic field allowed the investigation of the type of magnetic ordering and the nature of the magnetic interaction moment. Fig. 5 shows the evolution of the hyperfine magnetic field of sextets 1, 2 and 3 versus temperatures for $Bi_{0.9}Ba_{0.1}Fe_{0.9}[Ti0_{.95}(Yb_{0.5}Nb_{0.5})_{0.05}]_{0.1}O_3$ (x = 0.1). The hyperfine magnetic field gradually decreased, revealing a second order spin

Table 1
Hyperfine parameters extracted from in-situ Mössbauer measurements on $Bi_{1-x}Ba_xFe_{1-x}[Ti_{0.95}(Yb_{0.5}Nb_{0.5})_{0.05}]_xO_3$ ceramics with compositions x = 0 and x = 0.1.

Composition (x)	Temperature (K)	Fe site	IS (mm/s)	QS (mm/s)	H (Tesla)	Abs. %	Attribution
x = 0.1	298 K	Sextet1	0.37	0.08	48	31	magnetic components
		Sextet2	0.37	−0.01	47	35	
		Sextet3	0.41	−0.004	38	29	
		Comp4	0.25	0.80	0	5	Secondary Phase
	348 K	Sextet1	0.36	0.07	47	32	magnetic components
		Sextet2	0.36	−0.01	46	33	
		Sextet3	0.4	−0.003	37	28	
		Comp4	0.22	0.80	0	5	Secondary Phase
	398 K	Sextet1	0.36	0.085	45	34	magnetic components
		Sextet2	0.36	−0.02	45	31	
		Sextet3	0.39	−0.005	36	30	
		Comp4	0.21	0.70	0	5	Secondary Phase
	448 K	Sextet1	0.35	0.07	44	38	magnetic components
		Sextet2	0.35	−0.015	44	29	
		Sextet3	0.39	−0.004	33	29	
		Comp4	0.2	0.75	0	4	Secondary Phase
	498 K	Sextet1	0.34	0.07	42	42	magnetic components
		Sextet2	0.34	−0.02	39	25	
		Sextet3	0.38	−0.0035	30	28	
		Comp4	0.2	0.7	0	5	Secondary Phase
	523 K	Comp1	0.30	0.06	24	78	magnetic component
		Comp2	0.25	0.38	–	13	BFO paramagnetic
		Comp 3	0.20	0.27	–	5	Secondary Phase
	548 K	Comp1	0.27	0.06	20	31	magnetic component
		Comp2	0.22	0,53	–	60	BFO paramagnetic
		Comp 3	0.15	0,26	–	5	Secondary Phase
	558 K	Comp1	0.22	0.06	19	30	magnetic component
		Comp2	0,20	0.46	–	61	BFO paramagnetic
		Comp 3	0.15	0.26	–	5	Secondary Phase
	568 K	Comp2	0.11	0.40	–	94	BFO paramagnetic
		Comp 3	0.12	0.84	–	6	Secondary Phase
x = 0	298 K	Sextet1	0.40	0.4	50	46	magnetic components
		Sextet2	0.39	−0.08	49	46	
		Comp3	0.39	0.85	0	8	Secondary Phase
	643 K	Comp1	0.12	0.41	–	93	BFO paramagnetic
		Comp1	0.11	0.85	–	7	Secondary Phase
	653 K	Comp1	0.11	0.41	–	93	BFO paramagnetic
		Comp1	0.15	0.85	–	7	Secondary Phase

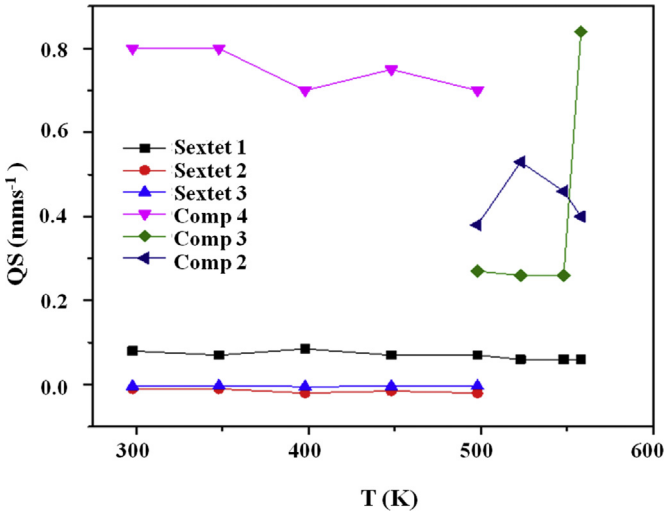

Fig. 4. Temperature dependence of the quadruple splitting of $Bi_{0.9}Ba_{0.1}Fe_{0.9}[Ti_{0.95}(Yb_{0.5}Nb_{0.5})_{0.05}]_{0.1}O_3$ (x = 0.1) ceramic.

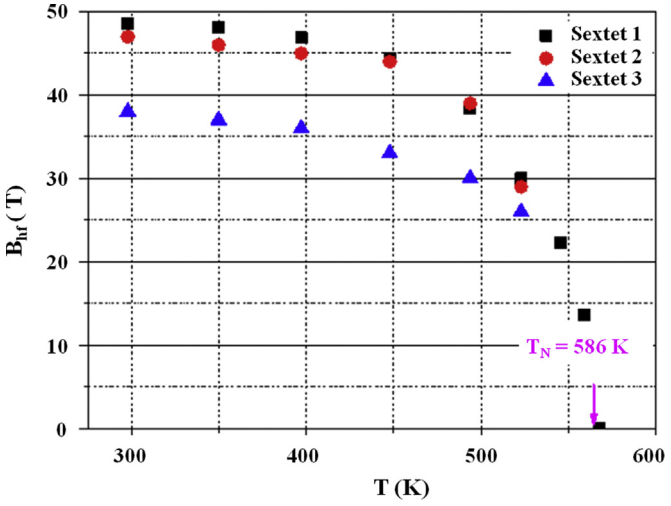

Fig. 5. A plot of the hyperfine magnetic field of sextets 1, 2 and 3 versus temperatures for $Bi_{0.9}Ba_{0.1}Fe_{0.9}[Ti_{0.95}(Yb_{0.5}Nb_{0.5})_{0.05}]_{0.1}O_3$ (x = 0.1).

rearrangement and tended to zero at the magnetic transition temperature T_N, revealing a paramagnetic behavior. The reduced magnetic hyperfine field H(T)/H(0 K) of each one of the three sextet components, as well as the averaged reduced magnetic hyperfine field as a function of the reduced temperature T/T_N is shown in Fig. 6. The value of the H(0K) was determined by extrapolation for each sextet and is of 52.82 T; 51.35 T and 43.78 T for sextet 1; 2 and 3, respectively. While all the three sextets and the average reduced magnetic hyperfine field showed the same pace of the theatrical curves of the Brillouin function for Fe^{3+} (S = 5/2), higher values

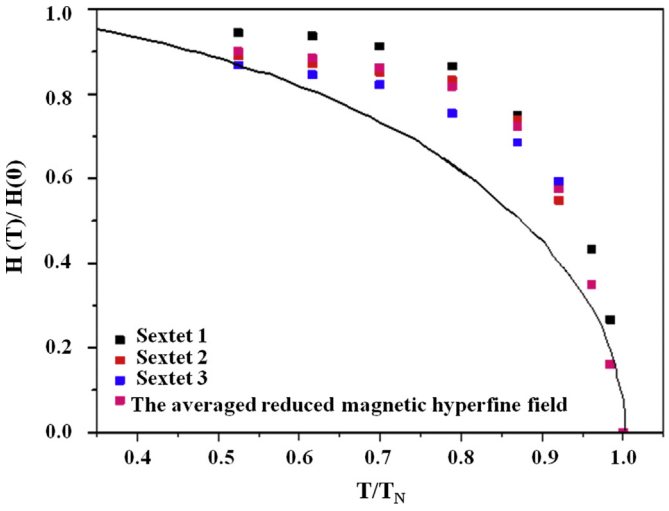

Fig. 6. The dependence of the reduced temperature T/T_N on the reduced magnetic hyperfine field H(T)/H(0K) of each one of the three sextet components (a) Sextet1; (b) Sextet2; (c) Sextet3 and (d) the averaged reduced magnetic hyperfine field for $Bi_{0.9}Ba_{0.1}Fe_{0.9}[Ti_{0.95}(Yb_{0.5}Nb_{0.5})_{0.05}]_{0.1}O_3$ (x = 0.1) ceramic. The full curve is the magnetization curve calculated with the Brillouin function for S = 5/2.

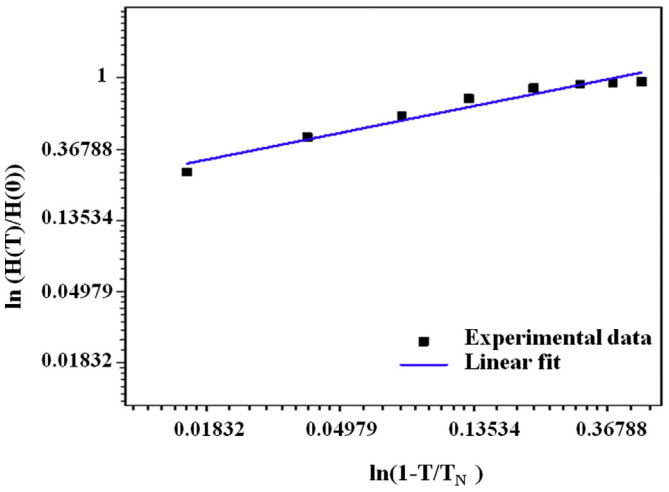

Fig. 7. The logarithm of the averaged reduced magnetic hyperfine field ln(H(T)/H(0 K)) plotted versus the logarithm of reduced temperature $\ln(1-T/T_N)$ for $Bi_{0.9}Ba_{0.1}Fe_{0.9}[Ti_{0.95}(Yb_{0.5}Nb_{0.5})_{0.05}]_{0.1}O_3$ (x = 0.1) ceramic.

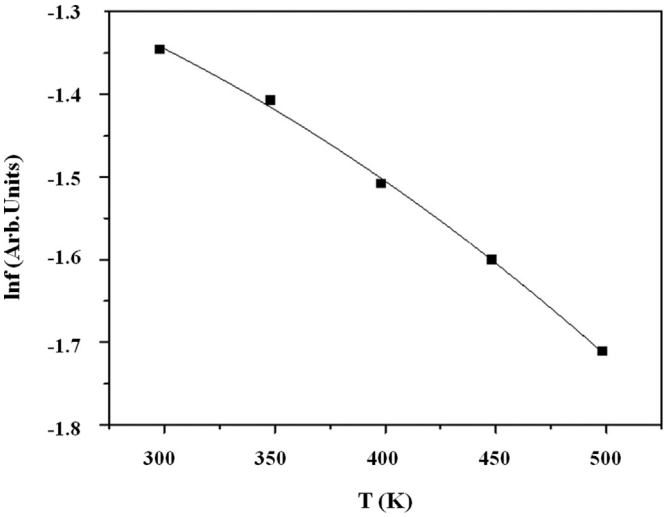

Fig. 8. Logarithm of the resonance absorption area, lnf versus temperatures for $Bi_{0.9}Ba_{0.1}Fe_{0.9}[Ti_{0.95}(Yb_{0.5}Nb_{0.5})_{0.05}]_{0.1}O_3$ ceramic.

compared to theatrical ones were obtained for $T/T_N > 0.5$, as reported for $BiFeO_3$ [40]. While a previous study of a polycrystalline Multiferroic Ba-doped $BiFeO_3$ [49] reported that this deviation from the Brillouin function is caused by the breaking of the antiferromagnetic super-exchange interaction between Fe^{3+}-O-Fe^{3+} as a result of the formation of oxygen vacancies, this factor cannot be the main origin of such a deviation seen the low amount of oxygen vacancies for our sample [25]. P. Fischer et al. [45] reported the proportionality between the evolution of hyperfine magnetic field deduced by Mössbauer spectroscopy and the sublattice magnetization temperature determined via neutron diffraction caused by magnetoelastic coupling. Thus, this deviation from Brillouin function for Fe^{3+} (S = 5/2) for our sample might be due to a spatially complicated spin structure as a result of the canting of antiferromagnetically ordered spins of undoped $BiFeO_3$, as the substituents Ba and Yb/Nb/Ti in A and B sites, respectively are non-magnetic [25], revealing magnetoelastic coupling. The logarithm of the averaged reduced magnetic hyperfine field ln(H(T)/H(0 K)) plotted versus the logarithm of reduced temperature $\ln(1-T/T_N)$ were adjusted in the asymptotic critical region below T_N, by the power law $H(T)/H(0\ K) = D(1-T/T_N)^{\beta}$ [40,41], as shown in Fig. 7. The value of the critical exponent β is of 0.375 ± 0.022 in the range of $0.01 < 1-T/T_N < 0.5$. This value is characteristic of a 3D magnetic long range order phase transition [57], in the same order to that reported by C. Blaauw et al. [40].

Fig. 8 shows the logarithm of the resonance absorption area, lnf versus temperatures for the $Bi_{0.9}Ba_{0.1}Fe_{0.9}[Ti0_{.95}(Yb_{0.5}Nb_{0.5})_{0.05}]_{0.1}O_3$ ceramic. The Debye temperatures were determined based on the temperature dependent resonance absorption area respecting the Debye approximation [46–49]. The obtained θ_D value was of 257 ± 21 K. $BiFeO_3$ previously showed a Debye temperature θ_D of 340 ± 50 K [40], which was higher than that of the θ_D for our x = 0.1 sample composition. This decrease of the Debye temperature implies the increase of the thermal capacity of the sample, defined as the quantity of energy which must be brought to increase its temperature by one Kelvin. This increase translates a greater thermal resistivity compared to $BiFeO_3$, reflecting a limitation of the problem of $BiFeO_3$ high conductivity [50]. This result is similar to the Mössbauer study of a polycrystalline Ba-doped $BiFeO_3$ compound [49] and that of Ho doped $BiFeO_3$ bulk ceramics [41]. It shows a Debye temperature of 321 K and 240 (80) K, respectively. With Ho doped $BiFeO_3$ bulk ceramics, this difference in the Debye temperature is attributed to the fact that different crystallographic sites in the same solid have different f -factors [45]. This is fully compatible with the choice of the three sextet component sites. Despite the fact that the measured θ_D corresponds to an average of the effective Debye temperature sites, we must not overlook it as a characteristic of the amelioration of thermal resistivity. While this change in the values of the magnetic transition temperature T_N and the Debye θ_D temperatures has been reported to be due to the change of the BFO lattice structure [51], more in-depth studies explained this change as the competition between antiferrodistortive and polar regions leading to a pseudo-colinear antiferromagnetic ordering rather than just a cycloidal spin modulation [52] as an influence of strained ferroic transition [52,53]. This predicts an amelioration of the piezoelectric properties [54], as a result of BFO substitution on both A and/or B sites, which is fully compatible with our previous report [25].

According to A. Agbelele et al. [55], the relation between the

sound velocity (v_S) in a crystal and its Debye temperature is determined by the following equation:

$$\theta_D = \frac{h\theta_s}{K}\left(\frac{3N}{4\pi V}\right)^{(1/3)} \quad (2)$$

Using this equation, the sound velocity in our $Bi_{0.9}Ba_{0.1}Fe_{0.9}[Ti_{0.95}(Yb_{0.5}Nb_{0.5})_{0.05}]_{0.1}O_3$ ceramic was deduced. V_S was of 5.5636 km/s. This value was a little higher than that reported for BFO ceramic at 300 K [56]. So, the sound velocity was more diffuse in our ceramic, highlighting the amelioration of acoustic properties. Therefore, $Bi_{0.9}Ba_{0.1}Fe_{0.9}[Ti_{0.95}(Yb_{0.5}Nb_{0.5})_{0.05}]_{0.1}O_3$ could be a good candidate of innovative optical applications. This average unpolarized sound velocity could be the main reason for the difference compared to polarized BFO ceramic [56] and a deeper study of polarized acoustic analysis can be a prospect to distinguish the longitudinal from transversal acoustic wave velocity and the modulation of the reflective index and to determine the elastic coefficients.

Fig. 9 shows the ^{57}Fe isomer shift plotted as a function of temperature for $Bi_{0.9}Ba_{0.1}Fe_{0.9}[Ti_{0.95}(Yb_{0.5}Nb_{0.5})_{0.05}]_{0.1}O_3$ (x = 0.1). Below T_N, the isomer shift of all the sextets is around 0.38–0.42 mms^{-1}, confirming again that irons are in a high-spin 3+ order state. As temperature increased, a little gradual decrease of δ was observed and a discontinuity of this magnetic hyperfine parameter, which appears at the magnetic transition temperature, is related to the change of the onset magnetic ordering [57]. This reveals the doping effect of non-magnetic Ba^{2+} and $Yb^{3+}/Nb^{5+}/Ti^{4+}$ in A and B sites, respectively in the BFO polycrystalline sample.

The evolution of the isomer shift versus temperature has been fitted for many base BFO samples using the Debye Model to determine the Debye temperature [46–56]. In our case, such fit was difficult to reach. This could be due to many factors such as the effect of strain, as mentioned by the logarithm of the resonance absorption area evolution, the complexity of the magnetic ordering, as previously interpreted on the hyperfine magnetic field evolution and as a cause of T_N shift compared to undoped BFO, and the effect of the magnetoelastic coupling to be proved by the dependence of XRD parameters versus temperatures. This static detailed ^{57}Fe Mössbauer study is an asset to a magnetic hyperfine investigation while a dynamic critical behavior must be more precise to study such a complex system and can be a subsequent study objective.

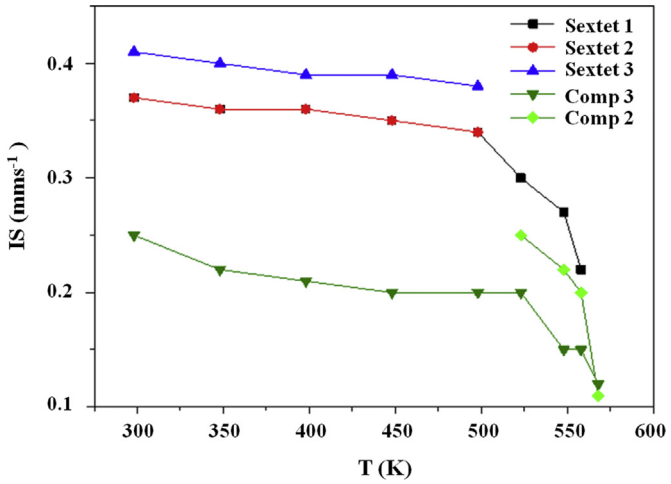

Fig. 9. The ^{57}Fe isomer shift plotted as a function of temperature in $Bi_{0.9}Ba_{0.1}Fe_{0.9}[Ti_{0.95}(Yb_{0.5}Nb_{0.5})_{0.05}]_{0.1}O_3$ (x = 0.1).

3.2. X-ray diffraction

Fig. 10 (a) shows the XRD patterns of $0.9BiFeO_3$-$0.1Ba[Ti_{0.95}(Yb_{0.5}Nb_{0.5})_{0.05}]O_3$ ceramic sample as a function of temperature. The patterns for all temperatures indicated a single phase perovskite structure and no parasite phase. In fact, at room temperature, XRD showed that this sample crystallizes in a tetragonal distorted perovskite structure with space group *P4mm* as previously reported [20]. While at room temperature, the $0.9BiFeO_3$–$0.1BaTiO_3$ sample has been reported to crystallize in Rhomboedral structure with the *R3c* space group [58,59], $BaTi_{0.95}(Yb_{0.5}Nb_{0.5})_{0.05}O_3$ has previously been shown to exhibit tetragonal symmetry [60]. Thus, since $BaTi_{0.95}(Yb_{0.5}Nb_{0.5})_{0.05}O_3$ is responsible for the ferroelectricity character, it is clear that the evolution structure was dominated by distortion due to doping ferroelectric cations. Therefore, all peaks were similar to that reported at room temperature and could be indexed based on a tetragonal perovskite structure, as shown in Fig. 10 (a). This predicts an isostructural phase transition around the magnetic transition temperature T_N (detected by ^{57}Fe Mössbauer spectroscopy). The profile matching refinement was done for all diffractograms. It agrees with the *P4mm* tetragonal space group structure. The values of the lattice parameters and the obtained unit cell volume are illustrated in Fig. 10(d). These parameters increased with increasing temperature. Similar isostructural behavior was reported for multiferroic BFO polycrystalline based samples [56,57]. It is important to note an anomaly in the temperature dependence of the lattice parameters and the unit cell volume around the magnetic transition temperature. These results are similar to the $(1-x)BiFeO_3$–$xBaTiO_3$ perovskite system [58–61] revealing a magnetoelastic coupling.

Rietveld refinements using neutron powder diffraction data of $(Bi_{0.8}Ba_{0.2})(Fe_{0.8}Ti_{0.2})O_3$ ceramic have been reported to exhibit a Rhomboedral structure distortion with a maxim distortion around T_N: the change in atomic positions allowing the calculation of the ionic polarization versus temperature indicates utmost ionic polarization around the magnetic transition temperature T_N [23]. This gives a direct evidence for atomic level magnetoelectric coupling in this multiferroïc BF-0.2BT. Also, A. Singh et al. [58] reported an isostructural phase transition with a significant shift in the atomic positions around the magnetic transition temperature as a direct evidence of magnetoelectric coupling for multiferroïc $0.9BiFeO_3$–$0.1BaTiO_3$ polycrystalline. More precisely, since Bi is largely responsible for the ferroelectricity of $BiFeO_3$, the large change in its position around the magnetic transition temperature confirms the coupling of ferroelectric and magnetic order parameters [55]. In this context, Rietveld refinement was done for long X-ray measurements at temperatures T = 300 K; 550 K, 560 K, 570 K and 580 K. Fig. 10 (b) and (c) show XRD results at room temperature T = 300 K (before the magnetic transition temperature T_N) and T = 580 K (after T_N), as examples. Fig. 10 (e) shows the shift positions of Bi^{3+}/Ba^{2+} and $Fe^{3+}/Ti^{4+}/Nb^{5+}/Yb^{3+}$ versus temperature obtained from Rietveld Refinement around T_N. In addition to the remarkable shift in the Bi^{3+} position around T_N, which is a first evidence of ferroelectric and magnetic order parameters coupling, the large shift of both Ba^{2+} and $Ti^{4+}/Yb^{3+}/Nb^{5+}$ compared to Fe^{3+} is a second evidence of magnetoelectric coupling, as $BaTi_{0.95}(Yb_{0.5}Nb_{0.5})_{0.05}O_3$ is responsible for the ferroelectricity character, as previously mentioned. Since the large changes in atomic positions entail the amelioration of electric polarization [23,24] around the magnetic temperature transition T_N, a pronounced magnetoelectric coupling is an evidence.

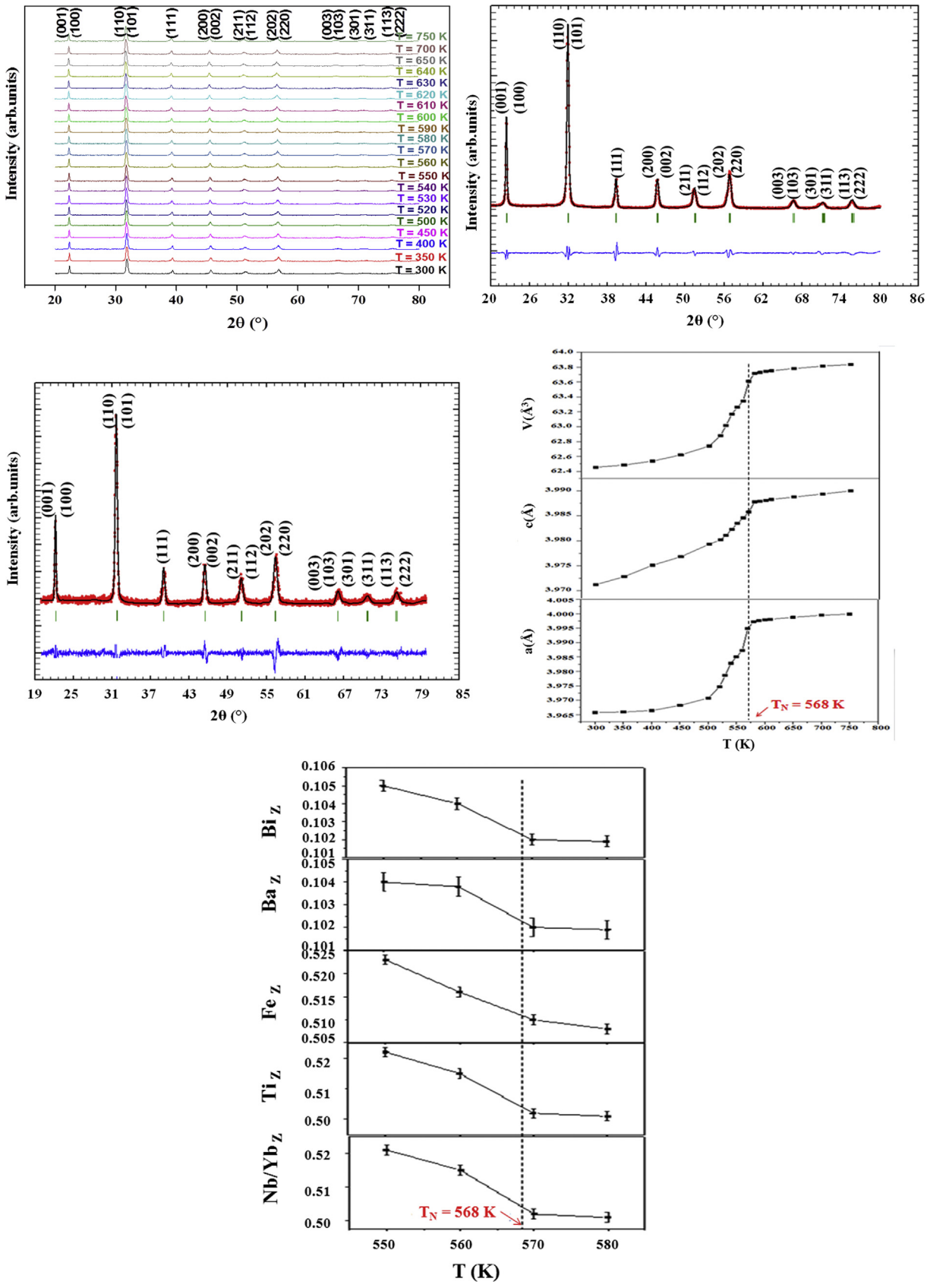

Fig. 10. (a) High temperature XRD patterns of the $0.9BiFeO_3$-$0.1Ba[Ti_{0.95}(Yb_{0.5}Nb_{0.5})_{0.05}]O_3$ sample.

3.3. Dielectric study

The observation of an anomaly of the dielectric properties at the magnetic transition temperature has widely been considered as an indirect evidence of magnetoelectric coupling of intrinsic multiferroïc origin. Such a result has been reported for both undoped [69] and doped [58,59,70–72] $BiFeO_3$ multiferroïc materials. The temperature dependence of the real part of dielectric permittivity and dielectric loss (tan δ) for $Bi_{0.9}Ba_{0.1}Fe_{0.9}[Ti_{0.95}(Yb_{0.5}Nb_{0.5})_{0.05}]_{0.1}O_3$ ceramic at 1 kHz are depicted in Fig. 11. In the temperature range from 303 K to 620 K, one peak is observed in both the real part of dielectric permittivity and dielectric loss (tan δ) curves. The temperature associated with this anomaly characterizes the magnetic transition temperature: $T_N = 568$ K as already highlighted by Mössbauer spectroscopy. This type of dielectric anomaly in magnetoelectrically ordered systems was predicted by the Landau-Devonshire theory of phase transition as an influence of magnetic order vanishing in the electric order [73,74]. This highlights that the transition from spin disordered state to spin ordered state affected the ferroelectric domain state and subsequently disturbed the ordered electric dipoles. Undoubtedly, such a dielectric behavior is an evidence of magnetoelectric coupling order for our $Bi_{0.9}Ba_{0.1}Fe_{0.9}[Ti_{0.95}(Yb_{0.5}Nb_{0.5})_{0.05}]_{0.1}O_3$ ceramic. Unfortunately, the ferroelectric to paraelectric transition could not be observed due to the limitations of the instruments as this transition is expected to be at a higher temperature.

Room temperature polarization hysteresis loops of $Bi_{0.9}Ba_{0.1}Fe_{0.9}[Ti_{0.95}(Yb_{0.5}Nb_{0.5})_{0.05}]_{0.1}O_3$ ceramic were recorded, as shown in Fig. 12. These electric hysteresis loops show that the saturated polarization cannot be achieved before breakdown. The comparison to a similar hysteresis loop with an unsaturated remnant polarization of 0.01 μC/cm^2 reported for undoped $BiFeO_3$ ceramic [75] demonstrate the enhancement of these electric properties, especially, with an attainable remnant polarizations of 0.229, μC/cm^2 for our doped ceramic. This prove the improvement of ferroelectric behavior and thus made an evidence of the reduced electric leakage for $Bi_{0.9}Ba_{0.1}Fe_{0.9}[Ti_{0.95}(Yb_{0.5}Nb_{0.5})_{0.05}]_{0.1}O_3$ ceramic, which is fully compatible with the increase of the maxim of the real part of dielectric permittivity and the decrease of dielectric loss for our ceramic compared to BFO.

3.4. Raman study

Raman scattering is a powerful technique to investigate the dynamic vibrational modes and the spin phonon coupling involving the structural phase transition [76–79], the magnetic exchange integral related to magnetoelastic properties [84,85] and the coupling between magnetic and ferroelectric order parameters [67,68].

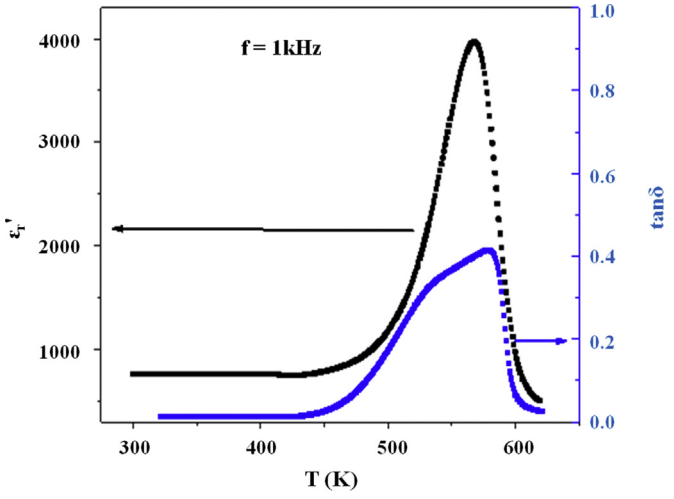

Fig. 11. Temperature dependence of the real part of dielectric permittivity and dielectric loss (tan δ) of $Bi_{0.9}Ba_{0.1}Fe_{0.9}[Ti_{0.95}(Yb_{0.5}Nb_{0.5})_{0.05}]_{0.1}O_3$ ceramic at 1 kHz.

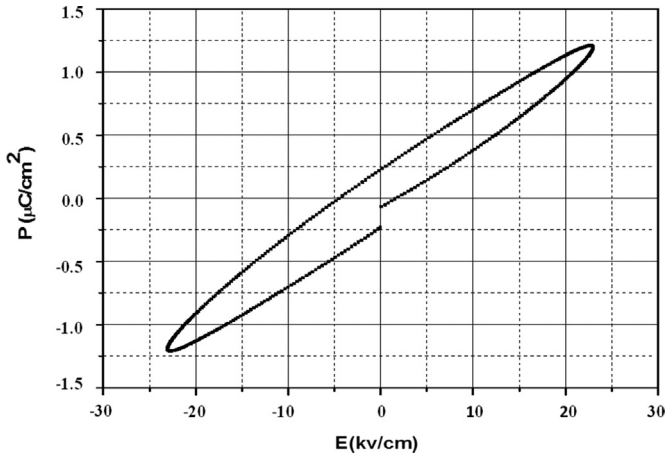

Fig. 12. Room temperature ferroelectric polarization hysteresis loops of $0.9BiFeO_3$-$0.1Ba[Ti_{0.95}(Yb_{0.5}Nb_{0.5})_{0.05}]O_3$ ceramic, measured at applied electric field, prior to electrical break down at a frequency of 10 Hz.

3.4.1. Room temperature Raman scattering investigation

According to the group theory for the undoped $BiFeO_3$ parent compound with Rhombohedral *R3c* structure at room temperature, thirteen optical modes were Raman active for the primitive cell units following this irreducible representation $\Gamma = 4A + 9E$ [85,86]. Fig. 13 shows the spectra for our synthesized $BiFeO_3$ ceramic. The assignment of the vibrational modes was based on a comparison with previous reports [82,83,86], as shown in Table 2. This comparison highlighted both first Raman order modes, at wavenumber below 960 cm^{-1}, and second Raman order modes at a higher frequency. Two things should be noted: first, the A_1 and E first Raman order modes, at low frequency, are relatively distinguishable, essentially the $A_{1\text{-}1}$, $A_{1\text{-}2}$ and $A_{1\text{-}3}$, at around 133.12 cm^{-1}, 172.24 cm^{-1}, 216.66 cm^{-1}, which have been related to Bi-O band

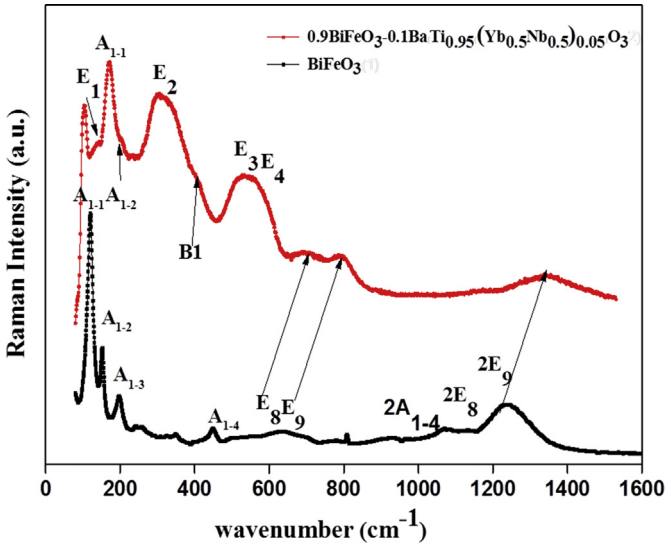

Fig. 13. Raman spectra of both $0.9BiFeO_3$-$0.1Ba[Ti_{0.95}(Yb_{0.5}Nb_{0.5})_{0.05}]O_3$ and $BiFeO_3$ ceramics reported at room temperature.

Table 2
Comparative Phonon frequency modes of $BiFeO_3$ based materials reported at room temperature.

Raman modes	M. K. Singh et al. [53] Calculated (Tetragonal *P4mm*)	M. K. Singh et al. [53] BFO thin film (Tetragonal *P4mm*)	M. K. Singh et al. [67] BFO thin film (Rhombohedral *R3c*)	G. L. Yuan et al. [72] BFO ceramic (Rhombohedral *R3c*)	Y. Yang et al. [74] BFO ceramic	Present study	
						x = 0	x = 0.1
A_{1-1}	129,8 cm^{-1} (TO_1)	136 cm^{-1} (LO_1) (TO_1)	136 cm^{-1}	126.1	139 cm^{-1}	133.12 cm^{-1}	168.54 cm^{-1}
A_{1-2}	155,7 cm^{-1} (TO_2)	168 cm^{-1} (LO_2) (TO_2)	168 cm^{-1}	165.5	172 cm^{-1}	172.24 cm^{-1}	174.24 cm^{-1}
A_{1-3}	206,0 cm^{-1} (TO_3)	212 cm^{-1} (LO_3) (TO_3)	211 cm^{-1}	213.0	217 cm^{-1}	216.66 cm^{-1}	
A_{1-4}	----------	----------	425 cm^{-1}	425	470 cm^{-1}	468.43 cm^{-1}	
B_1	332,6 cm^{-1} (TO)						407.29 cm^{-1}
E_1	125,6 cm^{-1} (TO_1)		275 cm^{-1}	111.7			135.98 cm^{-1}
E_2	245,4 cm^{-1} (TO_2)	257 cm^{-1} (TO_2)	335 cm^{-1}	259.5	262 cm^{-1}		308.47 cm^{-1}
E_3	453,6 cm^{-1} (TO_3)	464 cm^{-1} (TO_3)		339.6 cm^{-1}	275 cm^{-1}		521. 39 cm^{-1}
E_4	530,8 cm^{-1} (TO_4)	546 cm^{-1} (TO_4)	365 cm^{-1}	366.6 cm^{-1}	307 cm^{-1}		527.69 cm^{-1}
E_5			456 cm^{-1}	476.9 cm^{-1}	345 cm^{-1}		547.82 cm^{-1}
E_6			549 cm^{-1}	530.9 cm^{-1}	429 cm^{-1}		
E_7			597 cm^{-1}	599.6 cm^{-1}	262 cm^{-1}		
E_8					521 cm^{-1}	546.23 cm^{-1}	677.18 cm^{-1}
E_9					613 cm^{-1}	614.45 cm^{-1}	776.01 cm^{-1}
$2A_{1-4}$					958 cm^{-1}	964 cm^{-1}	1090 cm^{-1}
$2E_8$					1050 cm^{-1}	1040 cm^{-1}	1335 cm^{-1}
$2E_9$					1250 cm^{-1}	1206 cm^{-1}	1494 cm^{-1}

[65,84]. The higher frequency E first order Raman bands are attributed to Fe-O bands [65,84]. Second, three two-phonon Raman modes $2A_{1-4}$, $2E_8$ and $2E_9$ at around 964 cm^{-1}, 1040 cm^{-1} and 1206 cm^{-1}, related to second order Raman bands, are coexisting, revealing the coupling between magnetic and ferroelectric order parameters [68,69].

At room temperature, our doped sample $0.9BiFeO_3$-$0.1Ba[Ti_{0.95}(Yb_{0.5}Nb_{0.5})_{0.05}]O_3$ (x = 0.1) exhibited a tetragonal structure with space group *P4mm* distorted unit cells (Z = 1). The selection rules for the Raman active modes of the primitive cell with space *P4mm* group symmetry predict only twelve active Raman modes following irreducible representation: $\Gamma = 3A_1 + B_1 + 4E$ [72]. Raman peaks were broad and could not be resolved from each other mainly because of the disordered overlap of Raman modes which could be due to the random occupancy of A and B site ions, to the overlap of unpolarized TO and LO modes and to the ceramic nature of the sample. The assignment of the vibrational E and A_1 modes was based on the comparison with $BiFeO_3$ polarized Raman spectra with pseudo-tetragonal symmetry [62]. Fig. 13 shows this Raman spectra assignment of $0.9BiFeO_3$-$0.1Ba[Ti_{0.95}(Yb_{0.5}Nb_{0.5})_{0.05}]O_3$ at room temperature. This assignment is in strong agreement with the tetragonal $BiFeO_3$ [62]. Several qualitative changes of the Raman spectra, at room temperature, could be discerned when comparing $0.9BiFeO_3$-$0.1Ba[Ti_{0.95}(Yb_{0.5}Nb_{0.5})_{0.05}]O_3$ (x = 0.1) to $BiFeO_3$ ceramic. The relative intensity of the A modes at a wavenumber above 300 cm^{-1} attributed to Bi-O (A_{1-1}, A_{1-2} and A_{1-3}) reveals a remarkable decrease of the relative intensity compared to undoped $BiFeO_3$. The observed Raman spectra changes show the effect of substituting Bi by Ba leading to the breaking of the Bi-O bond. This could be due to the decline in stereochemical activity of $6s^2$ lone pair electrons of Bi, leading to a sharp drop in the intensity of the A_{1-2} peak: This corresponds to the change of the ionic Bi-O band to covalent Ba/Bi-O bond. Both A_{1-1} and A_{1-2} are assembled in a single peak around 170 cm^{-1}. The vanishing of A_{1-3} assigned to the rotation of the octahedron of oxygen along the axis [111] was related to the structural distortion from the ideal cubic phase Pm3m [86–88]. Again, a remarkable shift of the modes to the high frequencies, as reported in Table 2, was noticed. Considering the average mass variation in A, at the harmonic oscillator approximation ($w = (k/M)^{1/2}$), $M_{<A>}$ increased from 208.9804 g/mol for undoped $BiFeO_3$ to 201.81636 g/mol for our sample with x = 0.1 composition. This shift to a higher wavelength predicts the increase of the force constant between atomic harmonic oscillators. This observation suggests that the short range interatomic force dominates over the long-range coulombic (ionic) force for x = 0.1 composition with a tetragonal structure. Additionally, although polycrystalline samples had a random grain orientation, which means mixed symmetry due to oblique phonon dispersion, the longitudinal (TO) and transverse (LO) Raman mode characters are useful to expected changes in a qualitative manner. In fact, the relatively sharp peak for undoped $BiFeO_3$ ceramic becomes quite wide for $0.9BiFeO_3$-$0.1Ba[Ti_{0.95}(Yb_{0.5}Nb_{0.5})_{0.05}]O_3$. This could be interpreted as the greater overlap of TO-LO splitting in the A_1-symmetry normal modes due to the heterogeneity as substituting Bi and Fe by Ba and Ti/Yb/Nb in A and B sites, respectively. This result is fully compatible with previous reports [59,68,81,82] and in coherence with the change of the crystallographic structure, revealed by RX measurement.

3.4.2. *Raman study as a function of temperature*

Micro-Raman spectroscopy measurements were recorded in backscattering configuration from 50 to 1500 cm^{-1} in the range of temperature from 303 K to 728 K, as shown in Fig. 14.

The evolution of Raman spectra versus temperature reveals the following:

(1) The overall shape of the spectra did not change notably in the range from 303 K to 553 K. This temperature behavior indicates that our ceramic retained its room-temperature structure, which was in agreement with the XRD aspect. The persistence of modes with only relative intensity variation, in this temperature range, predicts a polar microdomain rearrangement and the intensity decrease of all bands of first order Raman scattering (below 1000 cm^{-1}) indicates a more isotropic polar state. This observation is fully compatible with the evolution of XRD parameters showing a progressive rearrangement of atomic displacement to a more isotropic state.

(2) From T = 553 K to T = 628 K, progressive evolution Raman spectra reveal a gradual decrease in the intensities of the modes between 50 cm^{-1} to 1000 cm^{-1}. On the contrary, the modes showing second order behavior $2A_4$, $2E_8$ et $2E_9$ between 1000 cm^{-1} to 1500 cm^{-1} became pondering. This result predicts an isostructural evolution to a pseudo-centrosymmetric structure, for which first Raman order was relatively removed, highly related to microscopic magnetic rearrangement (at the proximity of the magnetic

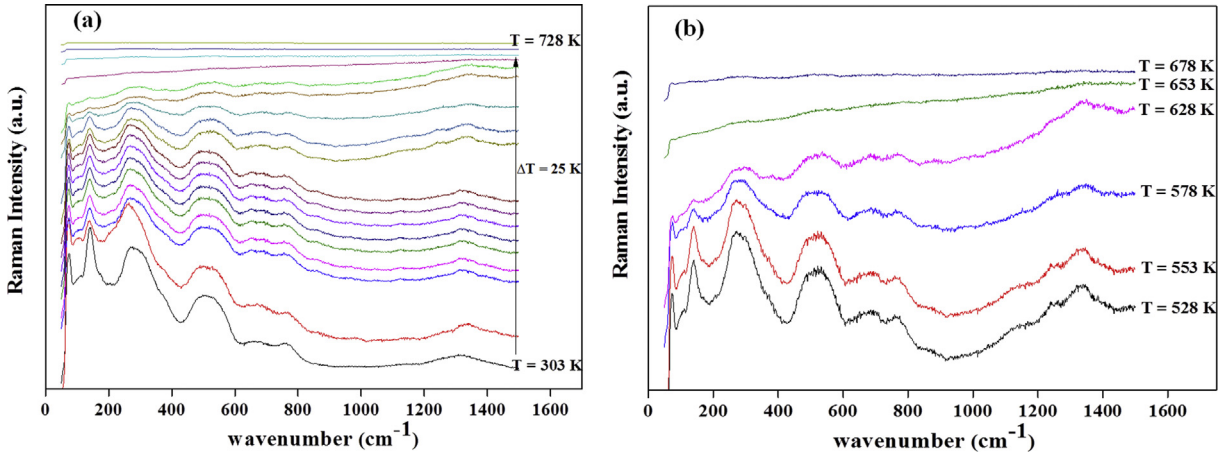

Fig. 14. Evolution of Raman spectra versus temperature for $0.9BiFeO_3$-$0.1Ba[Ti_{0.95}(Yb_{0.5}Nb_{0.5})_{0.05}]O_3$ ceramic (a) for the temperature range from T = 303 K to T = 728 K by with a step of ΔT = 25 K (b) for selected temperatures around magnetic phase and ferroelectric-paraelectric phase transition.

transition temperature). This result is fully compatible with the more symmetric Mössbauer spectrum evidence of more isotropic non-equivalent Fe site rearrangements in the crystal structure, as previously reported [66]. Seen the sensitivity around the magnetic transition temperature pointing out the strong two-spin phonon coupling [66], the Raman spectra from 800 to 1600 cm^{-1} in the range of temperature from 298 K to 758 K were recorded, as shown in Fig. 15 (a).

(3) Above T = 628 K, all the peaks vanished and the spectra became almost linear: such a spectra evolution could be linked to a structural phase transition to get a high temperature phase for which any first-order Raman scattering is forbidden. This change reveals a structural phase transition to cubic Pm3m symmetry. This observation is fully compatible with evolution of RX parameters versus temperatures: The lattice parameters a and c tend to have close values of about 3.99 Å around this temperature: this reveals a transition to a centrosymetrical paraelectric phase, which gives an idea of the ferroelectric-paraelectric T_c temperature phase transition value. All these changes display a combination between magnetic ordering and structural rearrangement revealing magnetoelastic coupling.

The A_1 mode, around 170 cm^{-1}, related to A-O banding [87,88], gradually decreases and vanishes around T = 653 K proving the change of the ferroelectric ordering and characterizing the ferroelectric transition temperature range.

Seen that the three two-phonon Raman modes centered at around 1000 cm^{-1} to 1300 cm^{-1} are reported to be very sensitive around the temperature magnetic transition pointing out the strong two-spin phonon coupling in undoped $BiFeO_3$ [64], the contribution of this two-phonon Raman spectrum versus temperature was analyzed here in order to understand the evolution at the proximity of magnetic transition temperature. In fact, seen that we studied unpolarized Raman ceramic spectra, to scrutinize the evolution of such modes, qualitative investigation was based on a virtual ion model or multimode model [78–80]. To discuss the evolution of the Raman signature around the magnetic transition temperature T_N = 568 K, it should be recalled that this magnetic transition is an isostructural phase transition (as previously proved by RX investigation). The overall Raman spectra shape is maintained across this temperature transition with a decrease of the relative intensity spectra modes. Nevertheless, a closer focus in the thermal Raman modes evolution reveals notable spectral changes around T_N, which is fully compatible with previous works [62–65].

In fact, since $2E_8$ and $2E_9$ has been attributed to Fe-O_1 and Fe-O_2 banding, for undoped $BiFeO_3$, which is critical of octahedral rotation origin of weak magnetization [65,77,78] and for our sample, the B site is occupied at the same time by Titanium Ti; Ytterbuim Yb; Niobium Nb and Iron Fe. We considered $2E_{8\text{-}1}$; $2E_{8\text{-}2}$; $2E_{9\text{-}1}$ and $2E_{9\text{-}2}$ modes as a simple model attributed to Ti/Yb/Nb-O_1; Fe-O_1; Ti/Yb/Nb-O_2 and Fe-O_2 banding as an attempt to understand the physical aspect of the vibrations. Fig. 15(a) shows the Raman spectrum versus temperature in the 800-1900 cm^{-1} wavenumber region. Fig. 15(b–g) shows some examples of fits, based on this model, for certain temperatures above and below magnetic transition temperature. The $A_{1\text{-}4}$ related to Bi/Ba-O band evolution did not show a significant change that could be related to the A site disorder. Fig. 16 reveals a significant evolution of the full width at half maximum FWHM and the Raman intensity ratio bands versus temperature as the result of the fit. This evolution reveals an anomaly around the magnetic transition temperature. This behavior has been extensively reported for multiferroic BFO based materials [64,65,68,77], as a proof of the coupling between magnetic and ferroelectric order parameters. A more in-depth observation showed switching of the relative maximum intensity of Fe-O_1 and Fe-O_2 band around 358 K, as if we have a new microscopic magnetic rearrangement. Below magnetic transition temperature and with increasing temperature, the two modes $2E_{8\text{-}2}$ and $2E_{9\text{-}2}$ decrease but tend to have a similar maximum vibration as if the two lengths tend to be symmetric, characterizing a paramagnetic state. Also, above magnetic transition temperature, $2E_{8\text{-}2}$ and $2E_{9\text{-}2}$ are less dominant than $2E_{8\text{-}1}$ and $2E_{9\text{-}1}$, as if the dominance of iron vibration modes responsible for magnetic aspect became a minority. Again, changes reveal magnetic and structural rearrangement linked to Fe/Nb/Yb/Ti-O gradual rearrangement. This leads to two modulations of the Fe-O-Fe band angle and hence an exchange interaction of the atomic displacement directly linked to polarization state: This undoubtedly proves magnetoelectric coupling. This result is fully compatible with XRD parameters behavior versus temperature and in-situ Mössbauer spectroscopy hyperfine settings around magnetic transition temperature.

4. Conclusion

We were able to prove magnetoelectric coupling of $0.9BiFeO_3$-$0.1Ba[Ti_{0.95}(Yb_{0.5}Nb_{0.5})_{0.05}]O_3$ ceramic prepared by the solid state

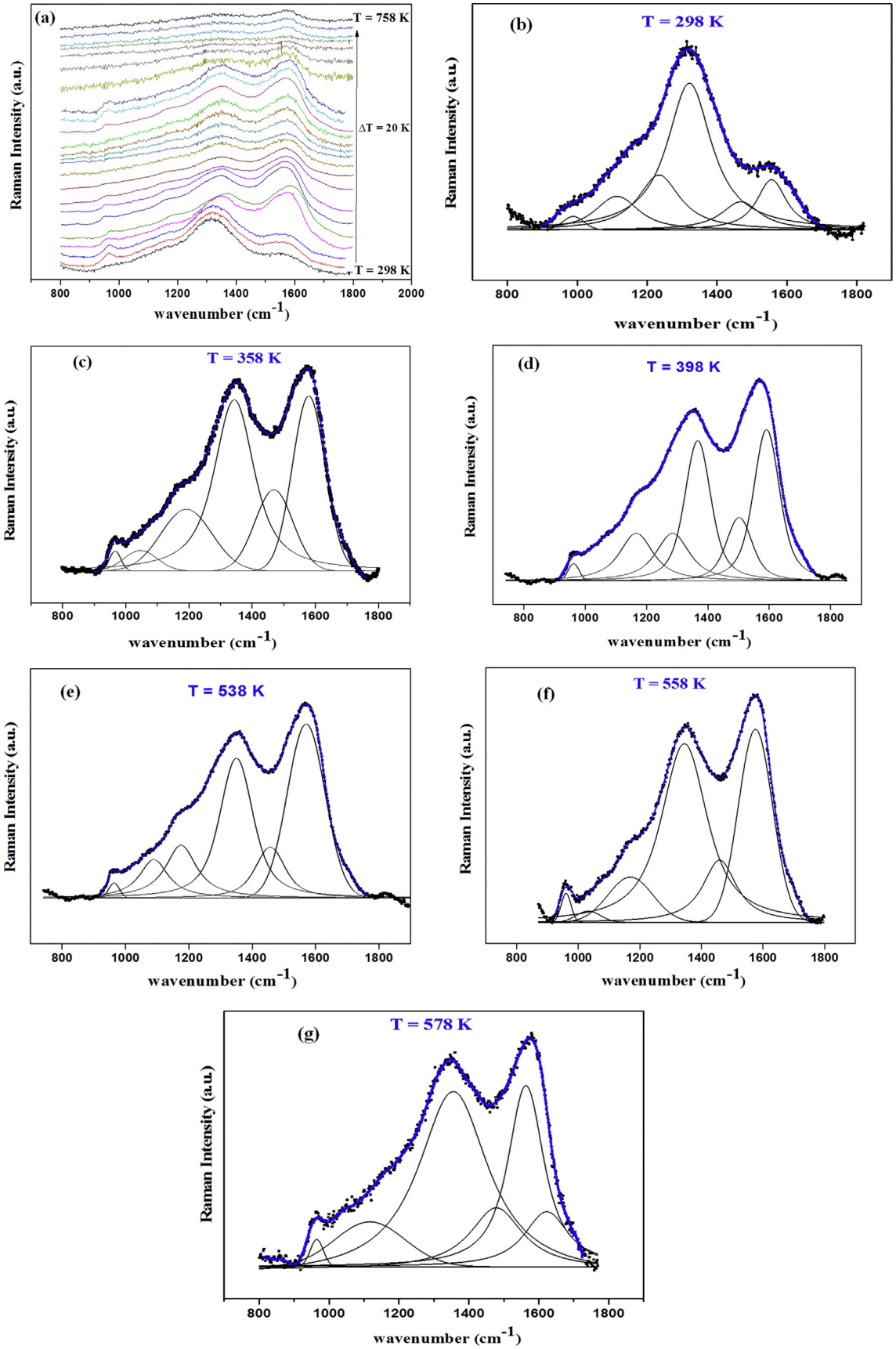

Fig. 15. (a) Detail of the Raman spectrum versus temperature in the 800-1900 cm^{-1} wavenumber region.

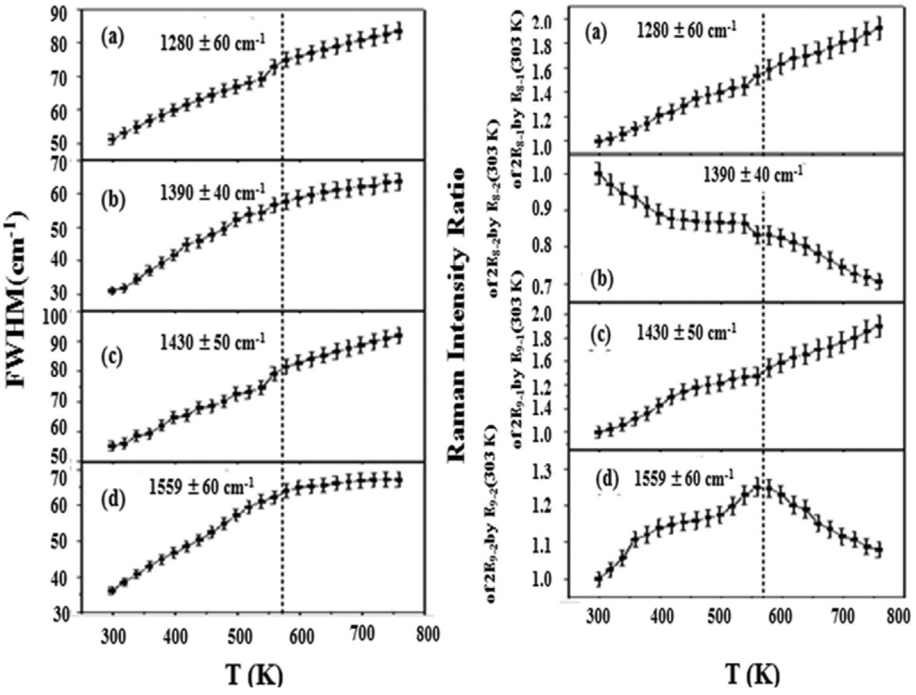

Fig. 16. Temperature dependence between 303 K and 758 K of the full width at half maximum FWHM and the Raman intensity ratio of each modes versus that at 303 K for (a) $2E_{8-1}$ modes at 1280 ± 12 cm^{-1}; (b) $2E_{8-2}$ modes at 1390 ± 11 cm^{-1}; (c) $2E_{9-1}$ modes at 1430 ± 8 cm^{-1} and (d) $2E_{9-2}$ modes at 1559 ± 17 cm^{-1}.

reaction method via in-situ Mössbauer spectroscopy, XRD, dielectric measurements and Raman scattering characterizations. In-situ Mössbauer spectroscopy in the temperature range of 300 K to 586 K showed the reduction of the magnetic transition temperature T_N to 568 K, as a result of the presence of different types of exchange constant that caused the weakening of $J_{Fe\text{-}Fe}$. The extracted hyperfine interaction parameters showed a 3D magnetic long range order phase transition with a complex spatial spin rearrangement as a result of the canting of antiferromagnetically ordered spins of $BiFeO_3$. The Debye temperature (θ_D) and the averaged sound velocity (V_S) were deduced to be of 257 ± 21 K and 5.5636 km/s, respectively. We thus highlighted that our doped sample may be a good candidate for piezoelectric devices as well as acoustic applications. XRD analysis, recorded for temperature range from 300 K to 750 K, reported an isostructural phase transition and showed an anomaly in the evolution of lattice parameters and the unit cell volume near the magnetic transition temperature T_N. Rietveld refinement revealed a significant shift in the atomic positions around T_N, specially for Bi/Ba atoms which are largely responsible for the ferroelectricity of $BiFeO_3$, thus proving the magnetoelastic coupling. The evolution of the real part of dielectric permittivity and dielectric loss (tan δ) versus temperatures at 1 kHz revealed an anomaly at 568 K that corresponds to the magnetic transition temperature T_N. The evolution of the Raman spectra in the temperature range from 303 K to 728 K revealed both magnetic rearrangement and atomic displacement leading to both modulating magnetic exchange interaction and polarization state. Drastic changes of the three two phonon modes centered at around 1000-1500 cm^{-1} revealed magnetic and structural rearrangement linked to Fe/Nb/Yb/Ti-O gradual rearrangement around magnetic transition temperature. All characterizations were fully compatible, revealing a clear coupling between magnetic and ferroelectric orders.

Rietveld refinement patterns at two temperature (b) T = 300 K (before the magnetic transition temperature T_N) and (c) T = 580 K (after T_N) (d) Evolution of the lattice parameters and the unit cell volume as a function of temperature and (e) Temperature variation of the shift positions of Bi^{3+}/Ba^{2+} and $Fe^{3+}/Ti^{4+}/Nb^{5+}/Yb^{3+}$, around T_N, obtained from Rietveld refinement.

Examples of fits made for certain temperatures: (b) T = 298 K; (c) T = 358 K; (d) T = 398 K; (e) T = 538 K; (f) T = 558 K and (g) T = 578 K.

References

[1] Ce-Wen Nan, M.I. Bichurin, Shuxiang Dong, D. Viehland, Multiferroic magnetoelectric composites: historical perspective, status, and future directions, J. Appl. Phys. 103 (3) (2008), https://doi.org/10.1063/1.2836410.

[2] J. Ma, J. Hu, Z. Li, C.-W. Na, Recent progress in multiferroic magnetoelectric composites: from bulk to thin films, Adv. Mater. 23 (9) (2011) 1062–1087.

[3] N.A. Hill, Why Are There so Few Magnetic Ferroelectrics? J. Phys. Chem. B 104 (2000) 6694–6709.

[4] R. Ramesh, N.A. Spaldin, Multiferroics: progress and prospects in thin films, Nat. Mater. 6 (2007) 21–29.

[5] S.W. Cheong, M. Mostovoy, Multiferroics: a magnetic twist for ferroelectricity, Nat. Mater. 6 (2007) 13–20.

[6] M. Bibes, A. Barthélémy, Multiferroics, towards a magnetoelectric memory: the room-temperature manipulation of magnetization by an electric field using the multiferroic $BiFeO_3$ represents an essential step towards the magnetoelectric control of spintronics devices, Nat. Mater. 7 (2008) 425–426.

[7] W. Eerenstein, N.D. Mathur, J.F. Scott, Multiferroic and magnetoelectric materials, Nature 442 (2006) 17, 05023-759-765.

[8] R. Ramesh, Thin Films: theory leads the way to new devices Computer simulations suggest a route to making a capacitor that can store electron spin, as well as charge, by applying an electric field to a conventional capacitor, Nat. Nanotechnol. 3 (2008) 7–8.

[9] A.K. Zvezdin, A.P. Pyatakov, Inhomogeneous magnetoelectric interaction in multiferroics and related new physical effects, Phys. Usp. 52 (8) (2009) 11–17.

[10] A.V. Zalesskii, A.K. Zvezdin, A.A. Frolov, A.A. Bush, ^{57}Fe NMR study of a spatially modulated magnetic structure in $BiFeO_3$, Condens. Matter J. Exp. Theor. Phys. Lett. 71 (11) (2000) 465–468.

[11] M.S. Bernardo, Synthesis, microstructure and properties of $BiFeO_3$-based multiferroic materials: a review, Boletín de la Sociedad Española de Cerámica y Vidrio 53 (1) (2014) 1–14, 0366-3175.

[12] A.M. Kadomtseva, Yu.F. Popov, A.P. Pyatakov, G.P. Vorobev, A.K. Zvezdin, D. Viehland, Phase transitions in multiferroic $BiFeO_3$ crystals, thin-layers, and ceramics: enduring potential for a single phase, room-temperature magnetoelectric 'holy grail', Phase Transit. 79 (12) (2006) 1019.

[13] W. Xing, Y. Ma, Z. Ma, Y. Bai, J. Chen, S. Zhao, Improved ferroelectric and leakage current properties of Er-doped $BiFeO_3$ thin films derived from

structural transformation, Smart Mater. Struct. 23 (2014), 085030–085031-9.
[14] H. Singh, A. Kumar, K.L. Yadav, Structural, dielectric, magnetic, magnetodielectric and impedance spectroscopic studies of multiferroic $BiFeO_3$–$BaTiO_3$ ceramics, Mater. Sci. Eng. B 176 (7) (2011) 540–547.
[15] Y. Ahn, J. Seo, J. Yeog Son, J. Jang, Enhanced multiferroic properties in epitaxial Yb-Doped $BiFeO_3$ thin films, Electron. Mater. Lett. 11 (4) (2015) 609–613.
[16] M. Zhong, G. Zhang, X. Yang, Preparation of Ti mesh supported WO_3/TiO_2 nanotubes composite and its application for photocatalytic degradation under visible light, Mater. Lett. 145 (2015) 216–218.
[17] G.L. Song, Y.C. Song, J. Su, X.H. Song, N. Zhang, T.X. Wang, F.G. Chang, Crystal structure refinement, ferroelectric and ferromagnetic properties of Ho^{3+} modified $BiFeO_3$ multiferroic, Alloys Compd. 696 (2017) 503–509.
[18] T. Zheng, J. Wu, Effects of site engineering and doped element types on piezoelectric and dielectric properties of bismuth ferrite lead-free ceramics, J. Mater. Chem. C 3 (2015) 11326–11334.
[19] J. Wu, Z. Fan, D. Xiao, J. Zhu, J. Wang, Multiferroic bismuth ferrite-based materials for multifunctional applications: ceramic bulks, thin films and nanostructures, Prog. Mater. Sci. 84 (2016) 335–402.
[20] T. Zheng, J. Wu, Quenched bismuth ferrite-barium titanate lead-free piezoelectric ceramics, J. Alloys Compd. 676 (2016) 505–512.
[21] J. Wu, D. Xiao, J. Zhu, Potassium–Sodium niobate lead-free piezoelectric materials: past, present, and future of phase boundaries, Chem. Rev. 115 (7) (2015) 2559–2595.
[22] T. Roisnel, Program Fullprof, Laboratoire de Chimie du Solide et Inorganique Moleculaire 4MR6511, CNRS-Universite de Rennes I, 2004. LLB-LCSIM, 2005, version 3.70. .
[23] A. Singh, A. Senyshyn, H. Fuess, T. Chatterji, D. Pandey, Neutron powder diffraction study of nuclear and magnetic structures of multiferroic $(Bi_{0.8}Ba_{0.2})(Fe_{0.8}Ti_{0.2})O_3$: evidence for isostructural phase transition and magnetoelastic and magnetoelectric couplings, Phys. Rev. B 83 (2011), 054406-1-9.
[24] D. Pandey, A. Singh, Structure, synthesis and multiferroic nature of $BiFeO_3$ and $0.9BiFeO_3$–$0.1BaTiO_3$: an overview, Bull. Mater. Sci. 32 (3) (2009) 361–367.
[25] A. Amouri, N. Abdelmoula, H. Khemakhem, Improved multiferroic properties in (1-x)BiFeO3–xBaTi0.95(Yb0.5Nb0.5)0.05O3 system ($0 \leq x \leq 0.3$), J. Magn. Magn. Mater. 417 (2016) 302–312.
[26] W.J. Merz, The electric and optical behavior of BaTiO3, single-domain crystals, Phys. Rev. 76 (1949) 1221–1225.
[27] I.A. Presniakov, A.V. Sobolev, I.O. Chernyavskii, D.A. Pankratov, I.V. Morozov, Anisotropic magnetic hyperfine interactions in phosphide FeP, Bull. Russ. Acad. Sci. Phys. 79 (8) (2015) 984–989.
[28] S.M. Selbach, T. Tybell, M.-A. Einarsrud, T. Grande, Size-dependent properties of multiferroic $BiFeO_3$ nanoparticles, Chem. Mater. 19 (26) (2007) 6478–6484.
[29] K. Sen, S. Thakur, K. Singh, A. Gautam, M. Singh, Room-temperature magnetic studies of La-modified $BiFeO_3$ ceramic, Mater. Lett. 65 (2011) 1963–1965.
[30] M.A. Ahmed, S.I. El-Dek, Optimizing the physical characterizations of orthoferrites to be used as pressure and gamma sensor, Mater. Lett. 60 (2006) 1437–1446.
[31] T. Durga Rao, R. Ranjith, S. Asthana, Enhanced magnetization and improved insulating character in Eu substituted $BiFeO_3$, J. Appl. Phys. 115 (2014), 124110-1-8.
[32] T. Durga Rao, T. Karthik, A. Srinivas, S. Asthana, Study of structural, magnetic and electrical properties on Ho-substituted $BiFeO_3$, Solid State Commun. 152 (2012) 2071–2077.
[33] T.D. Rao, S. Asthana, Evidence of improved ferroelectric phase stabilization in Nd and Sc co-substituted $BiFeO_3$, J. Appl. Phys. 116 (2014), 164102-1-8.
[34] A. Palewicz, T. Szumiata, R. Przeniosło, I. Sosnowska, I. Margiolaki, Search for new modulations in the $BiFeO_3$ structure: SR diffraction and Mössbauer studies, Solid State Commun. 140 (2006) 359–363.
[35] H. Fki, M. Koubaa, L. Sicard, W. Cheikhrouhou- Koubaa, A. Cheikhrouhou, S. Ammar-Merah, Influence of Y doping on structural, vibrational, optical and magnetic properties of $BiFeO_3$ ceramics prepared by mechanical activation, Ceram. Int. 43 (5) (2017) 4139–4150.
[36] J. De Sitter, C. Dauwe, E. De Grave, A. Govaert, On the Mössbauer parameters in $BiFeO_3$, Solid State Commun. 18 (5) (1976) 645–646.
[37] E. Jartych, A. Lisinska-Czekaj, D. Oleszak, D. Czekaj, Comparative X-ray diffraction and Mössbauer spectroscopy studies of $BiFeO_3$ ceramics prepared by conventional solid-state reaction and mechanical activation, Mater. Sci. Poland 31 (2) (2013) 211–220.
[38] A. Benali, M. Bejar, E. Dhahri, M. Sajieddine, M.P.F. Graça, M.A. Valente, Magnetic, Raman and Mössbauer properties of double-doping $LaFeO_3$, perovskite oxides, Mater. Chem. Phys. 149–150 (2015) 467–472.
[39] F. MENIL, Systematic trends of the ^{57}Fe Mössbauer Isomer shifts in (FeO_n) and (FeF_n) polyhedra. Evidence of a new correlation between the Isomer shift and the inductive effect of the competing bond T-X (Fe) (where x is o or F and T any element with a formal Positive charge), J. Phys. Chem. Solids 46 (7) (1985) 763–789. Review article7.
[40] C. Blaauw, F. van der Woude, Magnetic and structural properties of $BiFeO_3$, J. Phys. C Solid State Phys. 6 (1973) 1422–1431.
[41] P. Fischerl, M. Polomska, I. Sosnowskag, M. Szymanskig, Temperature dependence of the crystal and magnetic structures of $BiFeO_3$, J. Phys. C: Solid St. Phys. 13 (1980) 1931–1940.
[42] J.C. Jumas, J. O.-Fourcade, P. Lavela, J. Morales, J.L. Tirado, ^{119}Sn Mössbauer spectroscopy of some misfit layer sulfides, Chem. Mater. 7 (1995) 1193–1197.
[43] V.I. Goldanskii, E.F. Makarov, V.V. Khrapov, On the difference in two peaks of quadrupole splitting in Mössbauer spectra, Phys. Lett. 3 (7) (1963) 344–346.
[44] N. Sharma, A. Das, C.L. Prajapat, S.S. Meena, Spin reorientation behavior in $YMn_{1-x}M_xO_3$ (M =Ti, Fe, Ga; x =0, 0.1), J. Magn. Magn. Mater. 348 (2013) 120–127.
[45] P. Fischert, M. Polomskat, I. Sosnowska, M. Szymanski, Temperature dependence of the crystal and magnetic structures of $BiFeO_3$, J. Phys. C: Solid St. Phys. 13 (1980) 1931–1940.
[46] D.G. Rancourt, North-Holland, Accurate site populations from Mössbauer spectroscopy, Nucl. Instrum. Meth. Phys. Res. B44 (1989) 199–210.
[47] M. Ncube, D. Naidoo, K. Bharuth-Ram, D. Billing, H. Masenda, D.R. Sahu, B.K. Roul, R.M. Erasmus, XRD and Mössbauer spectroscopy study of Ho doped $BiFeO_3$, Hyperfine Interact. 219 (2013) 83–88.
[48] S. Bukshpan, Determination of the Debye temperature of SnTe using the Mössbauer effect in ^{119}Sn and ^{125}Te, Solid State Commun. 6 (1968) 477–478.
[49] W. Kim, C.S. Kim, Mössbauer study of a polycrystalline multiferroic Ba-doped $BiFeO_3$ compound, J. Kor. Phys. Soc. 56 (2) (2010) 607–610.
[50] G. Catalan, J.F. Scott, Physics and applications of bismuth ferrite, Adv. Mater. 21 (2009) 2463–2485.
[51] V.S. Pokatilov, A.S. Sigov, A.O. Konovalova, Mössbauer effect study of $Bi_{0.8}La_{0.2}FeO_3$ multiferroic on ^{57}Fe nuclei, Jetp Lett. 94 (9) (2011) 757–761.
[52] D. Sando, A. Agbelele, C. Daumont, D. Rahmedov, W. Ren, I.C. Infante, S. Lisenkov, S. Prosandeev, S. Fusil, E. Jacquet, C. Carrétéro, S. Petit, M. Cazayous, J. Juraszek, J.-M. Le Breton, L. Bellaiche, B. Dkhil, A. Barthélémy, M. Bibes, Control of Ferroelectricity and Magnetism in Multi-ferroic $BiFeO_3$ by Epitaxial Strain, Royal society publishing, 2017, pp. 1–8.
[53] C. Daumont, W. Ren, I.C. Infante, S. Lisenkov, J. Allibe, C. Carretero, S. Fusil, E. Jacquet, T. Bouvet, F. Bouamrane, S. Prosandeev, G. Geneste, B. Dkhil, L. Bellaiche, A. Barthelemy, M. Bibes, Strain dependence of polarization and piezoelectric response in epitaxial $BiFeO_3$ thin films, J. Phys. Condens. Matter 24 (16) (2012), 162202–1-5.
[54] M. Lejman, G. Vaudel, I.C. Infante, P. Gemeiner, V.E. Gusev, B. Dkhil, P. Ruello, Giant ultrafast photo-induced shear strain in ferroelectric $BiFeO_3$, Nat. Commun. 5 (4301) (2014) 1–7.
[55] A. Agbelele, D. Sando, I.C. Infante, C. Carrétéro, S. Jouen, J.-M. Le Breton, A. Barthélémy, B. Dkhil, M. Bibes, J. Juraszek, Insight into magnetic, ferroelectric and elastic properties of strained $BiFeO_3$ thin films through Mössbauer spectroscopy, Appl. Phys. Lett. 109 (2016), 042902-1-5.
[56] E.P. Smirnova, A. Sotnikov, S. Ktitorov, N. Zaitseva, H. Schmidt, M. Weihnacht, Acoustic properties of multiferroic $BiFeO_3$ over the temperature range 4.2–830 K, Eur. Phys. J. B 83 (2011) 39–45.
[57] H. Keller, I.M. Savié, Mössbauer studies of the static and dynamic critical behavior of the layered antiferromagnets $RbFeF_4$ and $KFeF_4$, Phys. Rev. B 28 (5) (1983) 2638–2650.
[58] A. Singh, V. Pandey, R.K. Kotnala, D. Pandey, Direct evidence for multiferroic magnetoelectric coupling in $0.9BiFeO_3$–$0.1BaTiO_3$, Phys. Rev. Lett. 101 (2008), 247602-1-247602-5.
[59] D. Pandey, A. Sing, Structure, synthesis and multiferroic nature of $BiFeO_3$ and $0.9BiFeO_3$–$0.1BaTiO_3$: an overview, Bull. Mater. Sci. 32 (3) (2009) 361–367.
[60] Z. Abdelkafi, N. Abdelmoula, H. Khemakhem, A. Simon, M. Maglione, Physical properties of new, lead free $BaTi_{1-x}(Nb_{0.5}Yb_{0.5})_xO_3$ ceramics, Ferroelectrics 371 (2008) 48–55.
[61] A. Singh, J. Prakash Patel, D. Pandey, High temperature ferroic phase transitions and evidence of paraelectric cubic phase in the multiferroic $0.8BiFeO_3$–$0.2BaTiO_3$, Appl. Phys. Lett. 95 (2009), 142909-1-142909-3.
[62] M.K. Singh, S. Ryu, H.M. Jang, Polarized Raman scattering of multiferroic $BiFeO_3$ thin films with pseudo-tetragonal symmetry, Phys. Rev. B 72 (2005), 132101, 132101-1-4.
[63] J.P. Patel, A. Singh, D. Pandey, Nature of ferroelectric to paraelectric phase transition in multiferroic $0.8BiFeO_3$–$0.2Pb(Fe_{1/2}Nb_{1/2})O_3$ ceramics, J. Appl. Phys. 107 (2010), 104115-1-7.
[64] R. Haumont, J. Kreisel, P. Bouvier, F. Hippert, Phonon anomalies and the ferroelectric phase transition in multiferroic $BiFeO_3$, Phys. Rev. B 73 (2006), 132101-1-4.
[65] M.O. Ramirez, M. Krishnamurthi, S. Denev, A. Kumar, S.-Y. Yang, Y.-H. Chu, E. Saiz, J. Seidel, A. P Pyatakov, A. Bush, D. Viehland, J. Orenstein, R. Ramesh, V. Gopalan, Two-phonon coupling to the antiferromagnetic phase transition in multiferroic $BiFeO_3$, Appl. Phys. Lett. 92 (2008), 022511-1-3.
[66] H. Fukumura, H. Harima, K. Kisoda, M. Tamada, Y. Noguchi, M. Miyayama, Raman scattering study of multiferroic $BiFeO_3$ single crystal, J. Magn. Magn. Mater. 310 (2) (2007) e367–e369.
[67] Y. Yang, J.Y. Sun, K. Zhu, Y.L. Liu, J. Chen, X.R. Xing, Raman study of $BiFeO_3$ with different excitation wavelengths, Physica B 404 (2009) 171–174.
[68] W. Zhong, R.D. King-Smith, D. Vanderbilt, Giant LO-TO splittings in perovskite ferroelectrics, Phys. Rev. Lett. 72 (22) (1994) 3618–3621.
[69] D. Kothari, V. Raghavendra Reddy, V.G. Sathe, A. Gupta, A. Banerjee, A.M. Awasthi, Raman scattering study of polycrystalline magnetoelectric $BiFeO_3$, J. Magn. Magn. Mater. 320 (2008) 548–552.
[70] H. Khelifi, I. Zouari, S. Habouti, N. Abdelmoula, D. Mezzane, H. Khemakhem, M. Es-Souni, Raman spectroscopy and evidence of magnetic transition in $0.9BiFeO_3$–$0.1Ba_{0.8}Sr_{0.2}TiO_3$ ceramic, J. Alloys Compd. 638 (2015) 50–54.
[71] B. Feng, H. Xue, Z.X. Xiong, Structure and multiferroic properties of Y-doped $BiFeO_3$ ceramics, Chin. Sci. Bull. 55 (4–5) (2010) 452–456.
[72] V.R. Palkar, D.C. Kundaliya, S.K. Malik, S. Bhattacharya, Magnetoelectricity at room temperature in the $Bi_{0.9-x}Tb_xLa_{0.1}FeO_3$ system, Phys. Rev. B 69 (2004), 212102-1-3.

[73] A.P. Cracknell, J. Lorenc, J.A. Przystawa, Landau's theory of second-order phase transitions and its application to ferromagnetism, J. Phys. C Solid State Phys. 9 (1976) 1731–1757.
[74] W. Cao, Constructing landau-Ginzburg-Devonshire type models for ferroelectric systems based on symmetry, Ferroelectrics 375 (2008) 1–12.
[75] M.M. Kumar, V.R. Palkar, K. Srinivas, S.V. Suryanarayana, Ferroelectricity in a pure $BiFeO_3$ ceramic, Appl. Phys. Lett. 76 (2000) 2764.
[76] M.N. Iliev, M.V. Abrashev, D. Mazumdar, V. Shelke, A. Gupta, Polarized Raman spectroscopy of nearly-tetragonal $BiFeO_3$ thin films, Phys. Rev. B 82 (2010), 014107-1-5.
[77] M.K. Singh, R.S. Katiyar, Phonon anomalies near the magnetic phase transitions in $BiFeO_3$ thin films with rhombohedral R3c symmetry, J. Appl. Phys. 109 (2011), 07D916-1-3.
[78] A. Palewicz, R. Przeniosło, I. Sosnowska, A.W. Hewat, Atomic displacements in $BiFeO_3$ as a function of temperature: neutron diffraction study, Acta Crystallograph. Section B 63 (2007) 537–544.
[79] A. Amouri, H. Abdelkefi, N. Abdelmoula, H. Khemakhem, Phase transition behavior and ferroelectric and vibrational properties of $(Na_{0.5}Bi_{0.5})_{1-x}Ba_x$-$Ti_{1-x}(Fe_{0.5}Nb_{0.5})_xO_3$ ceramics, J. Mater. Sci. 52 (7) (2016) 3876–3892.
[80] J. Suchanicz, I. J.-Sumara, T.V. Kruzina, Raman and infrared spectroscopy of $Na_{0.5}Bi_{0.5}TiO_3$ - $BaTiO_3$ ceramics, J. Electroceram. 27 (2011) 45–50.
[81] M.K. Singh, H.M. Jang, S. Ryu, M.-H. Jo, Polarized Raman scattering of multiferroic $BiFeO_3$ epitaxial films with rhombohedral R3c symmetry, Appl. Phys. Lett. 88 (2006), 042907-1-3.
[82] G.L. Yuan, S.W. Or, H.L. Chan, Raman scattering spectra and ferroelectric properties of $Bi_{1-x}Nd_xFeO_3$ (x = 0– 0.2) multiferroic ceramics, J. Appl. Phys. 101 (2007), 064101–1-5.
[83] S.K. Pradhan, Raman and electrical studies of multiferroic $BiFeO_3$, J. Mater. Sci. Mater. Electron. 24 (9) (2013) 3581–3586.
[84] Y. Yang, J.Y. Sun, K. Zhu, Y.L. Liu, L. Wan, Structure properties of $BiFeO_3$ films studied by micro-Raman scattering, J. Appl. Phys. 103 (2008), 093532-1-5.
[85] C. Ederer, N.A. Spaldin, Weak ferromagnetism and magnetoelectric coupling in bismuth ferrite, Phys. Rev. B 71 (2005), 060401-1-4.
[86] J. Bielecki, P. Svedlindh, D.T. Tibebu, S. Cai, S.G. Eriksson, L. Börjesson, C.S. Knee, Structural and magnetic properties of isovalently substituted multiferroic $BiFeO_3$: insights from Raman spectroscopy, Phys. Rev. B 86 (2012), 184422-1-15.
[87] R. Seshadri, N.A. Hill, Visualizing the role of Bi 6s "lone pairs" in the off-center distortion in ferromagnetic $BiMnO_3$, Chem. Mater. 13 (2001) 2892–2899.
[88] S.K. Pradhan, Raman and electrical studies of multiferroic $BiFeO_3$, J. Mater. Sci. Mater. Electron. 24 (9) (2013) 3581–3586.